Eur. Phys. J. B **35**, 531–549 (2003)
DOI: 10.1140/epjb/e2003-00307-0

THE EUROPEAN PHYSICAL JOURNAL B

Nonlinear effects and shock formation in the focusing of a spherical acoustic wave

Numerical simulations and experiments in liquid helium

C. Appert[1,a], C. Tenaud[2], X. Chavanne[1], S. Balibar[1], F. Caupin[1], and D. d'Humières[1]

[1] Laboratoire de Physique Statistique de l'ENS, associé au CNRS et aux Universités Paris 6 et 7, 24 rue Lhomond, 75231 Paris Cedex 05, France
[2] Laboratoire d'Informatique pour la Mécanique et les Sciences de l'Ingénieur, UPR CNRS 3251, B.P. 133, 91403 Orsay Cedex, France

Received 27 November 2002 / Received in final form 11 July 2003
Published online 24 October 2003 –

Abstract. The focusing of acoustic waves is used to study nucleation phenomena in liquids. At large amplitude, nonlinear effects are important so that the magnitude of pressure or density oscillations is difficult to predict. We present a calculation of these oscillations in a spherical geometry. We show that the main source of nonlinearities is the shape of the equation of state of the liquid, enhanced by the spherical geometry. We also show that the formation of shocks cannot be ignored beyond a certain oscillation amplitude. The shock length is estimated by an analytic calculation based on the characteristics method. In our numerical simulations, we have treated the shocks with a WENO scheme. We obtain a very good agreement with experimental measurements which were recently performed in liquid helium. In addition, the comparison between numerical and experimental results allows us to calibrate the vibration of the ceramic used to produce the wave, as a function of the applied voltage.

PACS. 67.40.-w Boson degeneracy and superfluidity of 4He – 43.25.+y Nonlinear acoustics – 62.60.+v Acoustical properties of liquids

1 Introduction

Recent experiments have shown that acoustic waves can be used to study the nucleation of phase transitions far from equilibrium under very clean conditions [1–3]. Thanks to hemispherical piezo-electric transducers, we have focused 1 MHz acoustic waves in liquid helium and produced large pressure and density oscillations. These waves are quasi-spherical and, at the acoustic focus (the center), their amplitude can be very large. We used an optical method to detect the nucleation of bubbles by the negative swings of the waves [1,2]. This nucleation occurs beyond a certain threshold in the sound amplitude which needs to be determined as accurately as possible, in order to compare with independent theoretical predictions. We later obtained evidence for the nucleation of crystals by the positive swings [3] and had the same need.

In the absence of nonlinear effects, the measurement of the nucleation threshold would be simple to do. For example, one could study the nucleation as a function of the static pressure in the experimental cell, and then use a linear extrapolation [2]. However, we expect nonlinear effects to occur, especially in cavitation studies. Indeed, the homogeneous nucleation of bubbles occurs near the "spinodal limit" where the compressibility diverges and the sound velocity vanishes. When the amplitude of an acoustic wave is such that during the negative swings the sound velocity approaches zero, it is clear that the wave must be highly distorted. This kind of nonlinear effects has been already noticed by several authors [4–6].

We thus try to calculate the nonlinear focusing of the acoustic waves. We start with the spherical geometry, because in a first approximation, everything depends only on the radial distance r from the center. As we shall see (Sect. 2), this calculation still appears difficult because the focusing of acoustic waves leads to the formation of shocks at all amplitudes in a spherical geometry, and their treatment is not straightforward. We first obtain this result and the associated shock length from an analytic calculation which uses the methods of characteristics (Sect. 2.2). Our calculation extends the former work of Nemirovskii [6] to the spherical case, except that we neglect the coupling with heat modes. It is done in the spirit of Greenspan and Nadim's work [7], though in our case it is slightly more tricky due to the shape of the equation of state. We make it quantitative by using the equation of state of liquid

[a] e-mail: appert@lps.ens.fr

helium [8] which is well established. For weak oscillation amplitudes of the transducer, the pressure and velocity are calculated by solving the Euler equations using a finite difference method (Sect. 2.3), neglecting any shock forming with an infinitesimal amplitude within a distance from the center much smaller than our mesh size. At larger amplitude, not only shocks cannot be ignored, but we have found that they had to be handled very accurately in order to get sensible numerical results. Therefore, we have had to adapt a code devoted to shock simulation to the case of helium. We have chosen a code based on a WENO scheme (Sect. 2.4) because it does not require the arbitrary limiters found in some other methods. Eventually we obtain the amplitude of the density oscillation at the focus as a function of the amplitude of the waves generated by displacement of the ceramic surface. The frequency of the waves is 1 MHz as in the experiments. In parallel, we have built an experiment to measure the focusing in a quasi-spherical geometry. As explained in Section 3, the results of this experiment allow a precise comparison with our theoretical and numerical work [9,10]. We find that the shape of the acoustic wave is indeed distorted at high amplitude and very well described by our calculations, thus validating our numerical method. The final comparison with our calculation allows us to calibrate the efficiency of the ceramic. As described in our conclusion, this work should now be extended to different geometries. One of them is the hemispherical geometry where, according to other experimental results [2], nonlinear effects are apparently less important, an observation which needs to be understood and compared with future calculations.

2 Theory

2.1 Description of the model

Throughout this paper, we consider a spherical geometry. We take it as one-dimensional since the pressure and density fields only depend on the radial distance r.

In the case of liquid helium 4 at zero temperature, the equation of state has been obtained by three different methods (sound velocity extrapolations, density functional calculations, and Monte Carlo simulations) with similar results. Maris [8] uses the simple form to relate the pressure (P) to the density (ρ):

$$P - P_{\rm sp} = \frac{b^2}{27}(\rho - \rho_{\rm sp})^3, \qquad (1)$$

where $P_{\rm sp}$ and $\rho_{\rm sp}$ are respectively the pressure and the density at the spinodal point where the compressibility diverges, the sound velocity, $c_{\rm s} = b(\rho - \rho_{\rm sp})/3$, vanishes and the liquid becomes totally unstable against the formation of the vapor.

We also considered helium 3, a lighter liquid which is not superfluid except at very low temperature – i.e. below the achievable temperature in our experiment – and which obeys the same equation of state.

Table 1. Summary of the various reference scales used in the paper to obtain dimensionless quantities. The first three scales are the fundamental ones, the last ones are derived from them.

Physical quantity	Reference scale	Numerical value of the reference scale	
		^{4}He	^{3}He
time ($\times 10^{-6}$ s)	T	1	1
length ($\times 10^{-3}$ m)	$\lambda_0 = c_{\rm s0}T$	0.238	0.182
density (kg m^{-3})	$\rho_{\rm sp}$	94.18	53.50
velocity (m s^{-1})	$c_{\rm s0}$	238.3	182.5
pressure ($\times 10^5$ Pa)	$\rho_{\rm sp}c_{\rm s0}^2$	53.47	17.82
Dimensionless constants	**Definition**	**Numerical value**	
spinodal pressure	$\frac{P_{\rm sp}}{\rho_{\rm sp}c_{\rm s0}^2}$	-0.18031	-0.17697
density at $P = 0$	$\frac{\rho_0}{\rho_{\rm sp}}$	1.541	1.531
$C_{\rm o}$	$\frac{b\,\rho_{sp}}{3c_{\rm s0}}$	1.848	1.883

The values of the parameter b and of the density ρ_0 at $P = 0$, are 14.030 m^4 s^{-1} kg^{-1} and 145.13 kg m^{-3} for helium 4, and 19.262 m^4 s^{-1} kg^{-1} and 81.916 kg m^{-3} for helium 3 respectively. Note that the value of the spinodal pressure for helium 3 (-3.1534×10^5 Pa) is less negative than for helium 4 (-9.6435×10^5 Pa), which means that the inner cohesion of liquid helium 3 is weaker than for helium 4.

We neglected dissipation since our main goal was to compare with experiments in superfluid helium 4 which has zero viscosity and where the attenuation of sound vanishes in the low temperature limit [11]. At the temperatures considered in case of helium 3, the viscosity is very weak and is neglected, though this approximation would probably need to be better justified. Therefore, the numerical approximation considers the Euler equations.

In order to use a dimensionless form of the equations, we have chosen as a time scale the period of the wave T ($T = 1/f = 1$ μs for 1 MHz waves), as a length scale the wavelength at zero pressure $\lambda_0 = c_{\rm s0}T$ and as a density scale the spinodal density $\rho_{\rm sp}$. The scalings and the remaining dimensionless parameters are given in Table 1 for liquid helium 3 and 4.

If we now consider ρ as the dimensionless density and u as the dimensionless velocity of the fluid, the Euler equations are written as follows:

$$\partial_t \rho + u\partial_r \rho + \rho \partial_r u = \frac{-\theta \rho u}{r}$$
$$\partial_t u + u\partial_r u = -\frac{1}{\rho}\partial_r P, \qquad (2)$$

or, by using the conservative variables ρ and $q = \rho u$,

$$\partial_t \rho + \partial_r q = \frac{-\theta q}{r}$$
$$\partial_t q + \partial_r [q^2/\rho + P(\rho)] = \frac{-\theta q^2}{\rho r} \quad (3)$$

where θ is respectively 0, 1, or 2 in planar, axisymmetric cylindrical, or spherical geometry. The equation of state, governing the dimensionless pressure variations, reads:

$$P - \frac{P_{\rm sp}}{\rho_{\rm sp} c_{\rm s0}^2} = \frac{C_{\rm o}^2}{3}(\rho - 1)^3, \quad (4)$$

and the dimensionless sound speed is

$$c_s = C_{\rm o}(\rho - 1). \quad (5)$$

This implies in particular that the dimensionless sound speed $c_{\rm s} = 1$ for $P = 0$ $\rho = \rho_0$. Also the classical ratio $B/A = \rho_{\rm st}(\partial^2 P/\partial^2 \rho)_{\rm st}/(\partial P/\partial \rho)_{\rm st}$ [12] is given by $2\rho_{\rm st}/(\rho_{\rm st} - 1)$, where "st" labels the unperturbed (static) values. For $P = 0$, $B/A = 5.697$ for helium 4 and 5.766 for helium 3, values close to those of water at 60 °C or liquid hydrogen at 14 K. When P goes to $P_{\rm sp}$, B/A goes to ∞. Note that, in order to have simple notations, we use the same names for physical and reduced variables. In general, calculations will be performed with reduced variables, while numerical results and experimental parameters will be given as physical quantities.

Boundary conditions are imposed at the center ($r = 0$)

$$u(0, t) = 0, \quad (6)$$

and on the transducer surface ($r = L(t)$)

$$u(L(t), t) = -\omega \, \Delta x_0 \, \sin(\omega t) \, [1 - \exp(-t/1.5)]\,. \quad (7)$$

In all our simulations, the motion of the transducer surface is much smaller than a mesh size and it is sufficient to impose an oscillating velocity on the ceramic at a fixed position L_0. The exponential term represents the response time of the transducer. In the experiment the response time is rather equal to 8 μs. Here we took it shorter to have a more rapid convergence of the calculation to the steady regime. This has no effect on the final result, as our simulations will always be used in the stationary regime.

In the whole paper, all the calculations are based on Euler equations, for which shock waves do occur. We are aware that, in superfluids as helium 4, there is no shock wave strictly speaking. Actually, when a steep gradient appears, it is regularized by dispersion instead of dissipation. This means that modes propagate with a different velocity depending on their frequency, and thus highest frequency modes are expelled from the steep region. However, we assume that, as shocks form only in the focal region, and during a limited time, not too much momentum is lost locally due to dispersion, and that in a first approximation, a viscous or dispersive regularization of the shocks is equivalent (note that any numerical scheme able to handle shocks will always introduce either a dissipation or a dispersion term in order to make shocks regular, even if Euler equations do not contain any viscous term). Besides, as we shall see (Sect. 2.3.2), we do not need to describe the shock structure exactly, as we are above all interested in the relaxation part of the wave. We have found from our simulations that the negative pressure swing only depends very weakly on the numerical viscous regularization we use and thus on the shock amplitude near the focal point. Still, it would of course be interesting to be able to quantify further the effects of dispersion, and this could be the object of a further work.

Throughout the paper, we shall consider helium 4 unless it is explicitly specified that it is helium 3. In the next sections, we show that shock waves can occur in this system, and we compute the radius (denoted as shock length in the following) at which a shock wave occurs for various oscillation amplitudes Δx_0 of the transducer surface.

2.2 The method of characteristics

In the study of compressible fluids, the method of characteristics is a standard one [13]. It has already been used for helium in a planar geometry (see for example [6]).

Here we are interested in the shock length in spherical geometry, for the equation of state (1). In this paper we define the shock length as the distance *from the center* where the shock forms. We shall use the method of characteristics to predict a lower bound for the shock length.

2.2.1 Riemann invariants and characteristics

Let us first recall the principle of the method. Solving the Euler equations means knowing the density ρ and the velocity u everywhere within a certain domain of the (r, t) plane. In our case, the "characteristics" are two families of curves $\left\{\mathcal{C}_i^{(+)}\right\}_{i\in R}$ and $\left\{\mathcal{C}_i^{(-)}\right\}_{i\in R}$ parameterized by i, where the parameter i could for example be defined as the r-coordinate at which the characteristic intersects the axis $t = 0$ (see Fig. 1 for an illustration). Thus, $\mathcal{C}_i^{(+)}$ (resp. $\mathcal{C}_i^{(-)}$) refers to a single curve in the (r, t) plane, which belongs to the (+) family (resp. (−)), and has in our case a positive slope (resp. negative). Each family completely covers the (r, t) plane as i is varied. The two families of curves intersect each other. Then, instead of locating a point in the plane by its coordinates (r, t), it is equivalent to indicate which particular characteristics $\mathcal{C}_i^{(+)}$ and $\mathcal{C}_j^{(-)}$ intersect each other at this point. The point (r, t) will then equivalently be referred to as point (i, j).

These families are chosen so that, for each family $\left\{\mathcal{C}_i^{(k)}\right\}$ with $k = \pm$, there exists a quantity I_k called "Riemann invariant", which is a function of ρ and u, and obeys a simple evolution equation along any characteristic $\mathcal{C}_i^{(k)}$ of the family. If the value of I_k is known at one point of a characteristic $\mathcal{C}_i^{(k)}$ (for example at the initial time), then it is easy to compute it on the whole curve.

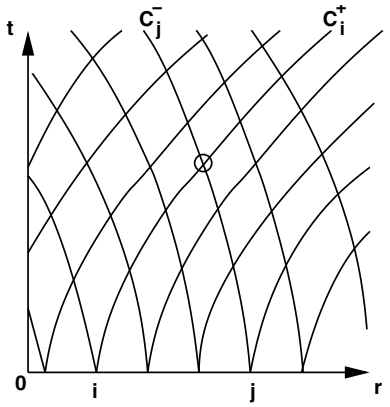

Fig. 1. The two characteristic families defined in the (r,t) plane. Here each curve is labeled by the r-coordinate of its intersection with the $t = 0$ axis. The point indicated by a small circle can be referred to either by its coordinates (r,t), or by the labels of the characteristics which intersect at this point (i,j).

As each point of the (r,t) plane is the intersection of two characteristics $\mathcal{C}_i^{(+)}$ and $\mathcal{C}_j^{(-)}$, we know the values of $I_+(\rho,u)$ and $I_-(\rho,u)$ at this point. Then the density ρ and the velocity u are entirely determined.

Now the precise form of the Riemann invariants and corresponding characteristics have to be derived from the Euler equations (2) and the equation of state for helium (4). The detailed calculations are given in Appendix A.1. Here we just give the results concerning the shape of the characteristics and the Riemann invariants. By definition, at any point, the slope of a characteristic $\mathcal{C}_i^{(+)}$ with equation $r = x(t)$ is $dx/dt = u + c_\mathrm{s}$ where u and c_s are taken at $(x(t),t)$. For a characteristic $\mathcal{C}_i^{(-)}$, it is $dx/dt = u - c_\mathrm{s}$. Using the dimensionless speed of sound c_s given by equation (5), the derivative along the characteristic reads

$$\frac{d}{dt} = \partial_t + (u \pm c_\mathrm{s})\partial_r.$$

The Riemann invariants are found to be

$$I_\pm \equiv C_\mathrm{o}(\rho - \ln\rho) \pm u, \tag{8}$$

and the equations verified by the "invariants" I_k $(k = \pm)$ are

$$\frac{d}{dt}\left[I_\pm\right] + \theta\frac{C_\mathrm{o}(\rho-1)u}{r} = 0 \tag{9}$$

where the derivative d/dt is taken along a characteristic $\mathcal{C}_i^{(k)}$. Again, θ is respectively 0, 1, or 2 in planar, cylindrical, or spherical geometry.

In planar geometry ($\theta = 0$), I_k is a true invariant, since it is constant along the corresponding characteristic, hence its name. In spherical or cylindrical geometries, it is not constant, due to the source term in equation (9), though it is still called an "invariant".

All this is valid at least as long as the characteristics belonging to the *same* family do not intersect each other. When they do, the corresponding I_k becomes multivalued. This is an indication that a shock has formed, and beyond the corresponding time, the description used in this section breaks down.

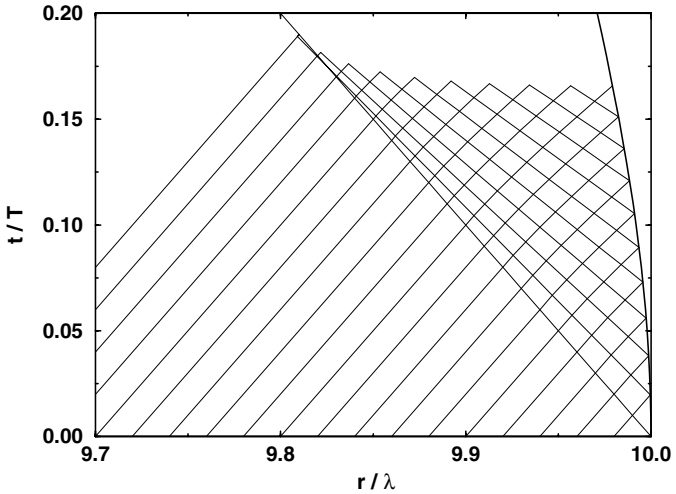

Fig. 2. Characteristics obtained for an experimental oscillation amplitude equal to $\Delta x_0 = 10$ μm, a cell radius $L_0/\lambda = 10$, and a time step $\delta t = 0.01$ T. The location of the piston is represented by the solid thick line on the right. On the upper left, two characteristics are crossing each other and the program stops. We chose a much larger oscillation than in the experiment, in order to have a rapid shock formation, and thus a readable picture.

2.2.2 Lower bound for the shock length - Analytic calculation

We shall now show that such an intersection does occur in the system, and calculate the corresponding shock length. We consider a spherical domain bounded by a spherical piston. At $t = 0$, the fluid is at rest with a density ρ_st and the piston surface is a sphere of radius L_0. As long as the fluid is at rest, all the characteristics are straight lines (see Fig. 2). The respective slopes of the characteristics $\left\{\mathcal{C}_i^{(+)}\right\}_{i\in R}$ and $\left\{\mathcal{C}_i^{(-)}\right\}_{i\in R}$ are $+c_\mathrm{st}$ and $-c_\mathrm{st}$, c_st being the sound velocity for the initial density ρ_st. The piston starts to move at $t = 0$ with a velocity $v_p(t) = -\Delta v_0 \sin(\omega t)$.

We denote $\mathcal{C}_0^{(-)}$ the characteristic originating from $r = L_0$ at $t = 0$, with slope $-c_\mathrm{st}$. The domain to the left of $\mathcal{C}_0^{(-)}$ is unperturbed unless some characteristic $\mathcal{C}_i^{(-)}$ crosses $\mathcal{C}_0^{(-)}$, i.e. unless there is a shock.

The aim of this calculation is to find an upper bound for the time necessary to form a first shock in the system. As the piston moves, it emits some characteristics which will cut $\mathcal{C}_0^{(-)}$ after a while, leading to a shock. We only study how the characteristics emitted at early times, and almost parallel to $\mathcal{C}_0^{(-)}$, will eventually cross it. Of course, some other characteristics emitted later could cross $\mathcal{C}_0^{(-)}$ earlier, or some shocks could occur somewhere else at earlier times. That is why our calculation only gives an upper

bound for the shock time given by

$$t_{\rm shock} \leq \frac{L_0}{c_{\rm st}} \left\{ 1 - \exp\left[-\frac{c_{\rm st}^2}{2\, L_0\, \omega\, \Delta v_0} \, \frac{\rho_{\rm st} - 1}{\rho_{\rm st} - \frac{1}{2}} \right] \right\} \leq \frac{L_0}{c_{\rm st}}, \tag{10}$$

(see Appendix A.2 for the details of the calculation). As the corresponding shock length $r_{\rm shock}$ is measured from the center of the sphere, a lower bound for $r_{\rm shock}$ is

$$L_0 \geq r_{\rm shock} \geq L_0 \exp\left[-\frac{c_{\rm st}^2}{2\, L_0\, \omega\, \Delta v_0} \, \frac{\rho_{\rm st} - 1}{\rho_{\rm st} - \frac{1}{2}} \right] > 0. \tag{11}$$

From this study we conclude that in spherical geometry, there is *always* formation of a shock, whatever the velocity of the piston is, as long as it has a nonzero acceleration towards the center of the sphere. However, when the oscillation amplitude $\Delta x_0 = \Delta v_0/\omega$ goes to zero, the lower bound of the shock length goes also to zero. If we assume that the lower bound is an accurate estimate of the actual shock position (assumption confirmed numerically in the next section), then, as shocks appear at the intersection of tangential characteristics, their initial amplitude is zero. If they are formed very near the center, their amplitude does not have time to grow much. This is true especially because of the existence of a cut-off: the notion of shock becomes meaningless when the width of the shock becomes of the same size as the shock length itself. So, as the oscillation amplitude tends to zero, the jump in density and velocity at the shock also vanishes, and their is no contradiction with the fact that the solution is expected to approach the linear solution [14].

2.2.3 Numerical calculation of the shock length

In order to show that the lower bound computed in the previous section is actually a good estimate of the shock length itself, let us now solve numerically the Euler's equations by computing a network of characteristics $\left\{\mathcal{C}_i^{(-)}\right\}_{i\in Z}$ and $\left\{\mathcal{C}_i^{(+)}\right\}_{i\in Z}$. As the fluid is at rest on the left of $\mathcal{C}_0^{(-)}$, we restrict our calculation to the (r,t) domain located between $\mathcal{C}_0^{(-)}$ and the piston trajectory.

Among the several possible parameterization choices, we have chosen for the (+) family the subset of characteristics crossing at regular time intervals t_i the first characteristic $\mathcal{C}_0^{(-)}$ emitted by the piston, where $t_i = i\delta t$, δt is an arbitrary fixed time step, and i is restricted to integer values (see Fig. 2).

When $\mathcal{C}_i^{(+)}$ meets the piston, a new characteristic $\mathcal{C}_i^{(-)}$ (with the same label i) is emitted from the piston at the same time. This defines the parameterization of the $(-)$ family. The intersection of the characteristics $\mathcal{C}_i^{(+)}$ and $\mathcal{C}_j^{(-)}$ is referred to as point (i,j).

During the nth step, we compute all the points (i,j) such that $i+j=n$ with i and j integers. Let us describe now how a point (i,j) can be computed from the points of the previous step (see Fig. 3). All the information comes

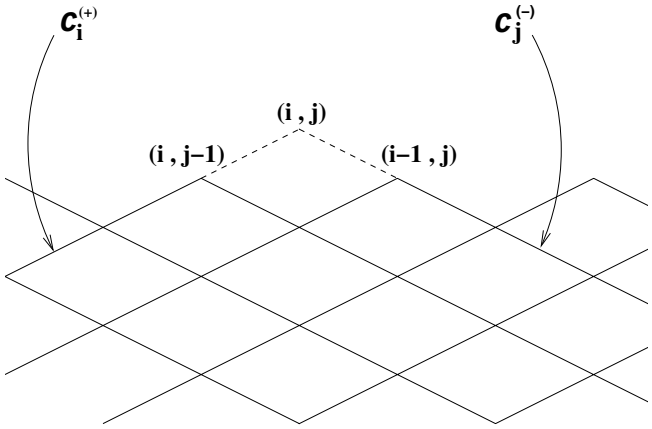

Fig. 3. Schematic representation of the network formed by the two families of characteristics, where i and j are integers.

from the two sites $(i,j-1)$ and $(i-1,j)$. We must extrapolate each characteristic $\mathcal{C}_i^{(+)}$ and $\mathcal{C}_j^{(-)}$ up to the next intersection (i,j). We compute the local slopes $u \pm c_{\rm s}$ of the characteristics $\mathcal{C}_i^{(+)}$ and $\mathcal{C}_j^{(-)}$ in sites $(i,j-1)$ and $(i-1,j)$ respectively. Then (i,j) is the intersection of the two straight lines which respectively go through $(i,j-1)$ and $(i-1,j)$ with these slopes.

The values of the Riemann invariants I_+ and I_- at (i,j) are found by numerical integration of the equations (8) and (9) along the two involved characteristics. From these values, both ρ and $q=\rho u$ are obtained.

The program stops whenever two characteristics of the same family cross each other, as shown in Figure 2. Then a shock occurs and the calculation based on characteristics breaks down (there would be multivalued points).

Let us now compare analytic and numerical results. Both calculations were done by taking L_0 equal to the experimental cell radius, i.e. 8 mm = 33.6 λ. We have also checked that the chosen time step $\delta t = 10^{-4}$ T is small enough to capture the shock length with a four digit accuracy. In Figure 4, we plot the shock distance $r_{\rm shock}$ measured from the center of the sphere as a function of the amplitude of the oscillation of the piston. We compare it with the analytic result. The agreement is excellent. This shows that our analytic calculation not only gives a lower bound but in fact a good estimate for the shock distance itself.

We have also performed the analytic calculation in the case of helium 3, neglecting the role of viscosity. It is expected that shocks form at smaller wave amplitude in helium 3, because, in this lighter liquid, the spinodal pressure is less negative than in helium 4.

2.3 Numerical simulations of Euler's equation

2.3.1 Numerical method

As we shall see now, a simple finite difference numerical scheme is sufficient to simulate our system with moderate amplitude, at least as long as the shock length is smaller

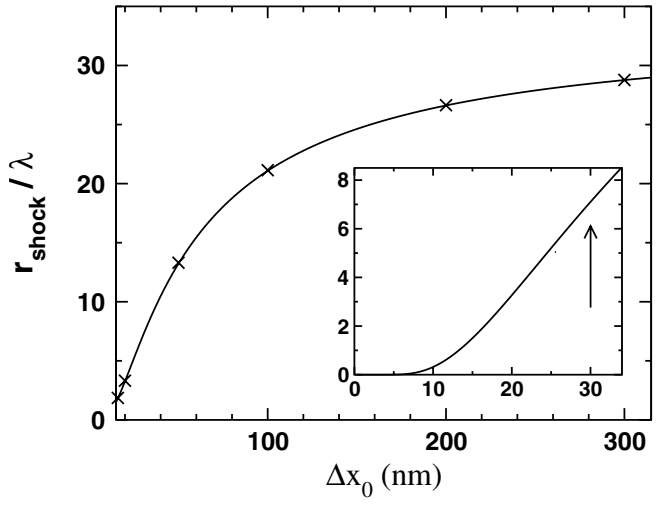

Fig. 4. Shock distance in helium 4 versus the amplitude of the oscillation on the ceramic, for a cell radius $L_0 = 33.6\lambda$, and a time step $\delta t = 10^{-4}$ T. We compare the analytic prediction (solid line) and our numerical calculations (symbols), both based on the characteristics method. The inset shows an expanded view for small amplitudes. The arrow indicates the amplitude for which cavitation is observed in the experiment at zero static pressure.

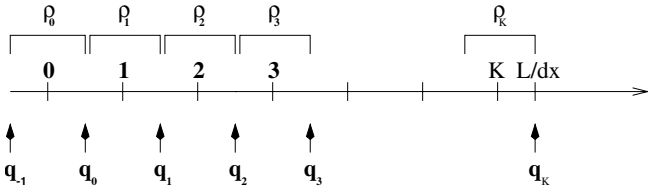

Fig. 5. Staggered lattice used for the numerical simulations. The radius of the simulation domain is $L = (K + 1/2)\,\delta r$. The symmetry with respect to the center $r = 0$ imposes $q_0 = -q_{-1}$, so that the velocity would vanish at the center: $q(r=0) = 0$.

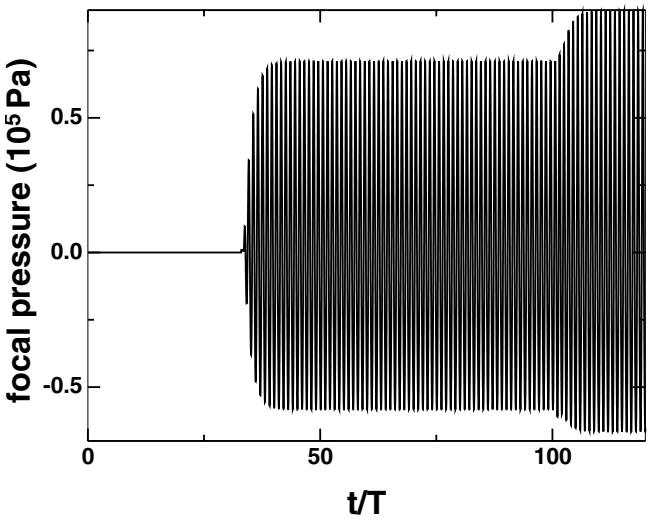

Fig. 6. Focal pressure for a weak oscillation $\Delta x_0 = 0.7$ nm. The simulation was done with 100 mesh points per wavelength and 10^4 points per period, starting with a static density $\rho_{\rm st} = \rho_0$, and thus a vanishing static pressure.

than the spatial discretization step. Our aim is to calculate numerically the pressure and density oscillation at the center. We chose to have two lattices, one for mass and the other for momentum. They are staggered (Fig. 5) and allow us to enforce exactly the conservation of mass in the volume $4\pi[(k+1/2)^3 - (k-1/2)^3]\delta r^3/3$:

$$\rho_k^{t+\delta t/2} = \rho_k^{t-\delta t/2} + \frac{\delta t}{\delta r}\frac{\left[\left(k-\frac{1}{2}\right)^2 q_{k-1}^t - \left(k+\frac{1}{2}\right)^2 q_k^t\right]}{k^2+\frac{1}{12}}. \tag{12}$$

We have taken the momentum equation in the form:

$$q_k^{t+\delta t} = q_k^t - \frac{\delta t}{\delta r}\left[\frac{(q_k^t+q_{k+1}^t)^2}{4\rho_{k+1}^{t+\delta t/2}} - \frac{(q_k^t+q_{k-1}^t)^2}{4\rho_k^{t+\delta t/2}}\right] - C_{\rm o}^2\left(\frac{\rho_k^{t+\delta t/2}+\rho_{k+1}^{t+\delta t/2}}{2}-1\right)^2\frac{\rho_{k+1}^{t+\delta t/2}-\rho_k^{t+\delta t/2}}{\delta r}\delta t - 4\frac{\delta t}{\delta r}\frac{(q_k^t)^2}{\left(k+\frac{1}{2}\right)\left[\rho_k^{t+\delta t/2}+\rho_{k+1}^{t+\delta t/2}\right]}. \tag{13}$$

As we use a staggered lattice, we only have to specify the boundary conditions for the momentum. It is vanishing at the center of the sphere ($r = 0$), and thus the symmetry with respect to the center imposes $q_0 = -q_{-1}$ (see Fig. 5). On the other hand, the motion of the piston is implemented by

$$q_K(t) = -\rho_K\,\omega\,\Delta x_0\,\sin(\omega t)\,\left[1-\exp(-t/1.5)\right].$$

2.3.2 Focal pressure

In Figure 6, the focal pressure is represented as a function of time. It is calculated from the average density in the central cell. The results of Figure 6 were obtained for a cell length equal to the experimental one, i.e. $L_0 = 33.6\ \lambda$, an oscillation amplitude $\Delta x_0 = 0.7$ nm, and a zero static pressure. Then the reduced sound velocity is equal to 1, and the wave needs 33.6 time units to reach the center of the cell. We are interested in the steady regime, which is established around $t/T > 45$. For $t/T > 33.6$, the wave goes through the focal point and propagates towards the ceramic where it is reflected back to the focal point (for $t/T > 2 \times 33.6$). It reaches again the latter at $t/T = 100.8 = 3 \times 33.6$. Then we stop our measurements, to be consistent with the experiment, which uses short bursts.

As long as the oscillation amplitude of the ceramic is not too large, nonlinear effects are negligible far from the focal point. Even the focal pressure during the steady regime is nearly sinusoidal, and the positive swings are only slightly larger than the negative ones (Fig. 7).

We have checked that the amplitude of the density is well represented by the function $\sin(kr)/(kr)$, as predicted from the linear theory [14] (see Fig. 8).

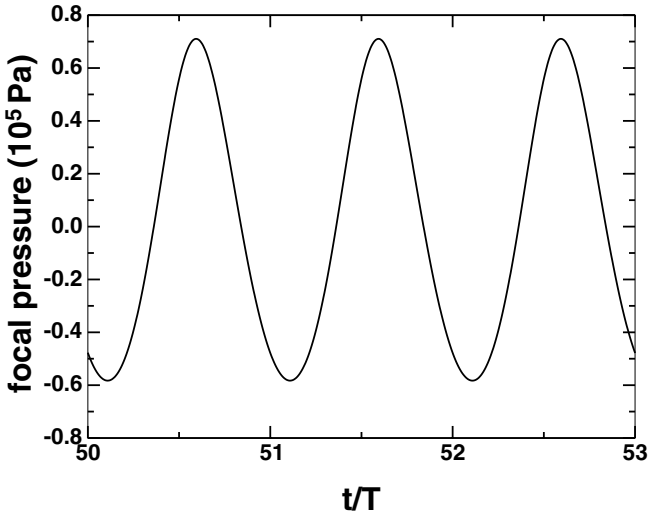

Fig. 7. Same figure as Figure 6, with a zoom on the steady state region. We are nearly in the linear regime.

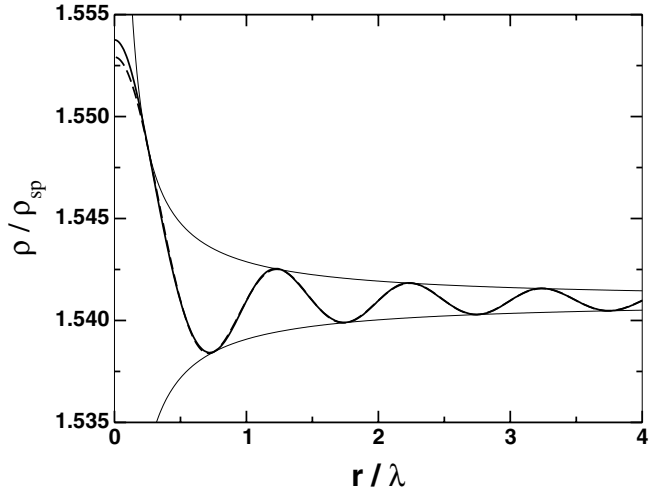

Fig. 8. Density profile for a weak oscillation $\Delta x_0 = 0.7$ nm (same simulation as in Fig. 6). We are still in the linear regime. The thin solid lines indicate a fit of the amplitude by $1/r$ and the dashed line a fit by $\sin(kr)/(kr)$. The latter is almost identical to the numerical result, except near the focal point where nonlinear effects become visible. The simulation was done with 100 mesh points per wavelength, starting with a static density $\rho_{\rm st} = \rho_0$ and thus a vanishing static pressure.

From our calculation of Section 2.2, we expect a shock to occur near the focal point. However, for the case of Figure 8, it happens on a region around $r = 0$ that cannot be seen because it is much smaller than the mesh size. Indeed, the predicted reduced shock length would be $r_c/\lambda = 4.2 \times 10^{-28}$, to be compared with the mesh size $\delta r/\lambda = 0.01$.

When Δx_0 is increased to 5 nm, nonlinear effects become more important. Although the reduced shock length (from the center) is equal to 0.003, thus still smaller than the spatial step $\delta r/\lambda = 10^{-2}$, one sees the formation of fronts (Fig. 9). At the center, the positive swings of the pressure are now much larger than the negative ones (Fig. 10).

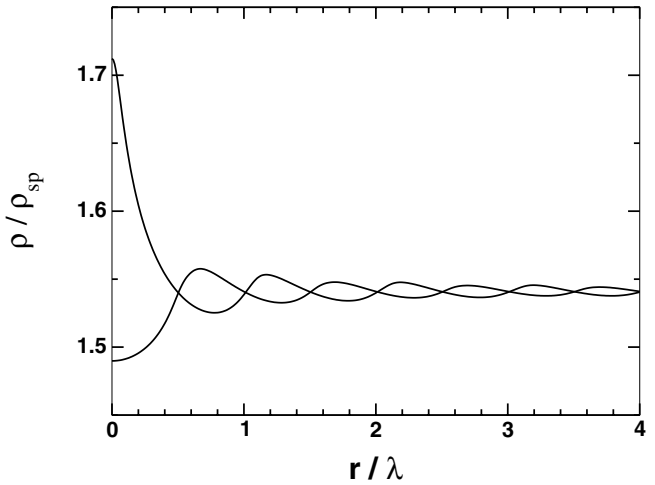

Fig. 9. Density profile for an oscillation $\Delta x_0 = 5$ nm, at different times, corresponding to the maximal and minimal focal pressure. Nonlinearities are becoming important. The simulation was done with 100 mesh points per wavelength and 10^5 points per period, starting with a static density $\rho_{\rm st} = \rho_0$.

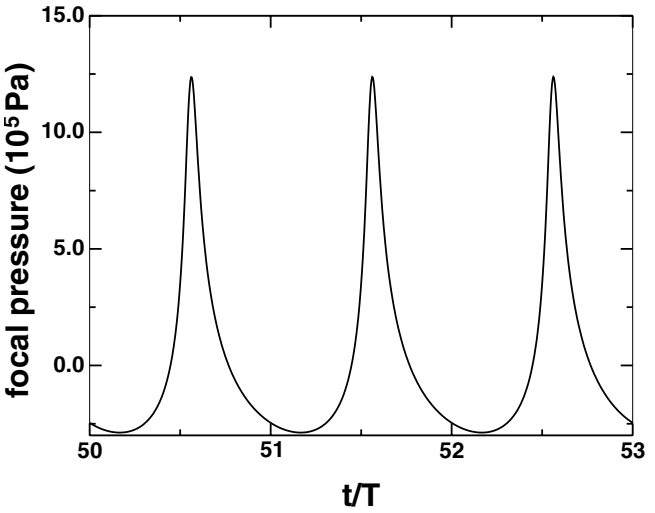

Fig. 10. Focal pressure for an oscillation $\Delta x_0 = 5$ nm in the same conditions as Figure 9. Note the important nonlinear positive swings.

There are two main sources for nonlinearities: the equation of state and the inertial terms in the Euler equations, both enhanced by the spherical geometry. Their relative importance have been studied by various simulations where we suppressed one of them. If we take a constant sound speed $c_{\rm s} = c_{\rm st}$, i.e. a linear equation of state, then nonlinear effects are strongly reduced and the maximal and minimal pressure excursions are almost symmetrical. If we rather suppress the inertial term $u\partial_r u$ from the Euler equation for the velocity, nonlinear effects are also reduced, but to a lesser extent.

Thus all nonlinear terms reinforce each other, but the dominant nonlinear effect comes from the equation of

Table 2. Maxima and minima of the focal pressure ($\times 10^5$ Pa) computed in three different cases. Case 1: full simulation of the equations (3). Case 2: the sound speed is kept constant $c_s = c_{st}$. Case 3: the inertial term $u\partial_r u$ is suppressed. All calculations are done for the same experimental oscillation amplitude $\Delta x_0 = 5.9$ nm, and for two different cell radii.

L_0 / λ_0	L_0 (mm)		case 1	case 2	case 3
10	2.38	P_{max}	13.53	6.18	11.92
		$P_{\min}$	–3.49	–4.83	–3.58
20	4.76	P_{max}	17.17	6.34	14.27
		$P_{\min}$	–3.31	–4.73	–3.41

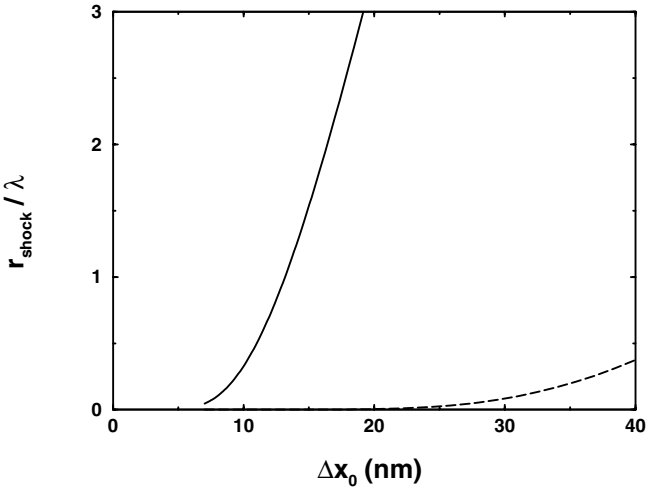

Fig. 11. Shock distance in helium 4 versus the amplitude of the oscillation of the ceramic. We compare the analytic prediction for the full equation of state (solid line) and the case of a constant sound speed (dashed line).

state, as summarized in Table 2 (the geometry also plays a crucial role of course, but it cannot be separated from the other effects). Note that the nonlinear effects increase also with the radius of the cell as it is well known.

This is confirmed if we do the analytic calculation of Section 2.2.2 again, now with a constant sound speed. We find then that

$$r_{\text{shock}} \simeq L_0 \exp\left[-\frac{c_{\text{st}}^2}{L_0 \omega \Delta v_0}\right]. \tag{14}$$

In Figure 11, we compare with the result (11) of Section 2.2.2 obtained with the full equation of state. It turns out that, for realistic oscillation amplitudes, the shock appears almost at the center if the nonlinearities of the equation of state are not taken into account.

2.4 Shock formation at large amplitudes. The WENO scheme

Eventually, when the amplitude Δx_0 is further increased, the formation of shocks can be observed in our simulations. The numerical scheme described in the previous section becomes unstable around $\Delta x_0/\delta r = 2 \times 10^{-3}$, and a new scheme had to be used.

For performing fine analysis of the Euler flow dynamics, non-dissipative high-order accurate schemes (like spectral [15–17] or Padé schemes [18,19]) have been identified as suitable tools as far as regular numerical solutions are searched. However, when dealing with compressible flows involving discontinuities, non-dissipative high-order schemes introduce spurious oscillations in the vicinity of the discontinuity and one must use a numerical scheme which can both represent the smooth regions of the solution with the minimum of numerical dissipation, and capture the discontinuities by using an *ad hoc* scheme with robust discontinuity-capturing features. Therefore, as shock waves may occur in the computational domain for the present calculations, the numerical method we use is based on a high-order intrinsically-dissipative scheme originally designed to capture discontinuities.

Among the shock capturing techniques found in the literature, Total Variation Diminishing (TVD) schemes are generally considered to be well suited for the capture of shock waves but too diffusive in smooth regions, due to the limitation of the accuracy to first-order near extrema. More recent schemes like the ENO (Essentially Non-Oscillatory) or WENO (Weighted Essentially Non-Oscillatory) family schemes [20–22] have been introduced to increase the order of accuracy in the smooth regions of the solution. Using such an approach, the derivatives of the flux function are approximated by means of high-order polynomial reconstruction over several grid points (the set of these points is named "stencil"). In the ENO/WENO schemes, to avoid spurious oscillation in the vicinity of the discontinuity, a selection mechanism is used to chose the most regular stencil among all the stencil candidates. The discrete solution is then obtained on a variable stencil at each grid point. One of the drawbacks in the generic ENO scheme is the necessity to check and choose between several stencil candidates, which is quite CPU consuming. To overcome this disadvantage, we preferred using a Weighted ENO scheme (WENO) since it improves the order of accuracy of the generic ENO scheme (by using a weighted combination of the stencil candidates) without increasing the computational cost [23]. This scheme is rapidly presented in the next section. Some more technical details about WENO scheme can be found in Appendix B or in the literature [22,23].

2.4.1 The shock-capturing method

For simplicity, the governing equations (3) are recast in the following abridged form:

$$\frac{\partial Q}{\partial t} = \mathcal{L}(r, Q) \tag{15}$$

where $Q = (\rho\ ,\ \rho\ u)^t$ is the vector of the conservative variables and

$$\mathcal{L}(r, Q) = -\frac{\partial F(Q)}{\partial r} + \mathcal{S}(r, Q)$$

stands for a spatial operator, applied on Q, based on both the Euler flux vector $F(Q) = \left(\rho\ u\ ,\ \rho\ u^2 + P\right)^t$ and the source term $\mathcal{S}(r,Q) = -\dfrac{\theta}{r}\left(\rho\ u, \rho\ u^2\right)^t$.

In view of the discretization of the Euler equations (15), we will denote by δt and δr the time step and cell width respectively. Q_i^n will denote the numerical vector solution at a time $t = t_0 + n\ \delta t$ and at a position $r = i\ \delta r$. For simplicity, the integration of these equations has been performed by means of a decoupled time and space algorithm.

a) Time integration

The time integration is performed by means of a third-order accurate Runge-Kutta method, proposed by Shu and Osher [21], chosen because this high-order accurate scheme does not increase the Total Variation of the right-hand-side of the equations ($\mathcal{L}(r,Q)$). When dealing with discontinuities, this Total Variation Diminishing (TVD) property is important since it ensures that no local extremum can be created during the time integration, meaning that no oscillation may occur in the vicinity of the shock wave due to the time scheme. At each point of the computational grid, the time integration is then obtained via a multi-step algorithm as follows:

$$\begin{aligned} Q^{(0)} &= Q_i^n \\ Q^{(1)} &= Q^{(0)} + \delta t\ \mathcal{L}\left(Q^{(0)}\right) \\ Q^{(2)} &= \frac{3}{4}\ Q^{(0)} + \frac{1}{4}\ Q^{(1)} + \frac{1}{4}\delta t\ \mathcal{L}\left(Q^{(1)}\right) \\ Q^{(3)} &= \frac{1}{3}\ Q^{(0)} + \frac{2}{3}\ Q^{(2)} + \frac{2}{3}\delta t\ \mathcal{L}\left(Q^{(2)}\right) \\ Q_i^{n+1} &= Q^{(3)}. \end{aligned} \tag{16}$$

The explicit Runge-Kutta scheme exhibits a stability condition based on the CFL number: CFL $= \mu\ \delta t/\delta r$, where μ is the maximal value of the eigenvalues μ_i^k of the Euler flux Jacobian $(\partial F/\partial Q)_i$ (see Appendix B). All the calculations presented herein have been obtained by considering a fixed value of the CFL number, namely CFL $= 0.5$, which corresponds to a nearly optimal value for the considered Runge-Kutta scheme. Let us mention that this value ensures a good representation of all the time scales of the flow under study.

b) Spatial integration

The spatial discretization of the right-hand-side term $\mathcal{L}(r,Q)$ of equation (15) is obtained by means of a high-order finite volume scheme:

$$\mathcal{L}(r_i, Q_i^n) = -\frac{1}{\delta r}\left[\overline{F}^n_{i+1/2} - \overline{F}^n_{i-1/2}\right] + \mathcal{S}(r_i, Q_i^n) \tag{17}$$

where $\overline{F}^n_{i+1/2}$ is the numerical flux evaluated at the cell interface $(r_{i+1/2})$. To reconstruct the numerical flux at the cell interfaces, a scheme with a discontinuity-capturing feature must be employed to prevent oscillations in the vicinity of the shock wave. Following a previous study [23] on the capability of some recent high-order shock capturing schemes to recover basic fluid mechanics phenomena, the numerical flux has been evaluated by means of a WENO scheme [22]. The numerical flux ($\overline{F}^n_{i+1/2}$) is approximated by using a polynomial reconstruction over a set of several grid points (the "stencil") around the cell boundaries, such that the flux derivatives is estimated with a $(2p-1)^{\text{th}}$-order of accuracy at best (in regular regions):

$$\frac{\partial F(Q)}{\partial r} = \frac{1}{\delta r}\left[\overline{F}^n_{i+1/2} - \overline{F}^n_{i-1/2}\right] + \mathcal{O}(\delta r)^{(2p-1)} \tag{18}$$

where p is the order of the ENO reconstruction procedure [21]. See Appendix B for more details in the flux reconstruction. In the followings, the calculations have been performed by using $p = 3$, leading to a fifth-order accuracy in regular regions while the order of accuracy is decreased close to unity in the shock region.

c) Boundary conditions

To solve the system of equations we need boundary conditions at the center of the sphere ($r = 0$) and at the ceramic surface ($r = L(t)$). At the center of the sphere, the fluid is at rest and we prescribe $u|_{i=0} = 0$ as mentioned in equation (6). The density is then calculated through the equation of mass conservation by assuming that the momentum is an antisymmetric quantity with respect to the sphere center. The singular behavior of the source term $\rho u/r$ requires a specific treatment at the sphere center since the momentum vanishes as r goes to zero. However, by noticing that the ratio $\rho u/r$ is a symmetric quantity, the first radial derivative of this ratio vanishes at the sphere center. By using a second order upwind difference, $(\rho u/r)|_{r=0}$ is estimated by using the interior points as:

$$\left(\frac{\rho u}{r}\right)_{i=0} = \frac{4}{3}\left(\frac{\rho u}{r}\right)_{i=1} - \frac{1}{3}\left(\frac{\rho u}{r}\right)_{i=2}. \tag{19}$$

At the ceramic surface, one has to impose a condition corresponding to the motion of the ceramic. In our case, as the displacement of the sphere does not reach a sonic velocity, the two eigenvalues μ^1 and μ^2 are of opposite sign. This means that the two pieces of information necessary to determine the two unknowns ρ and u come from opposite directions. In particular, at the boundary, one comes from the interior of the domain and the other from the outside. Thus, it is possible to prescribe one of the variables, and the other one would be determined by an upwind scheme, i.e. asymmetric towards the inner domain. However in the present problem, it is much more natural to prescribe the velocity at the ceramic surface given by equation (7).

2.4.2 Numerical results

Of course, all the results presented in Section 2.3.2 can be reproduced with our WENO scheme. Besides, one can increase further the oscillation amplitude. For $\Delta x_0 = 7\,\text{nm}$, the reduced shock length (from the center) is equal to 0.043, i.e. larger than the spatial step $\delta r/\lambda = 10^{-2}$, and

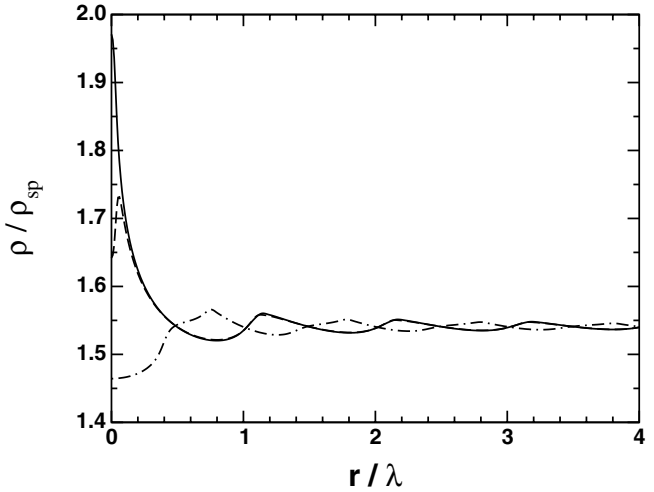

Fig. 12. Density profile for an oscillation $\Delta x_0 = 7$ nm, at different times, corresponding to the maximal (solid line), minimal (dot dashed line) focal pressure, and to a sharp front arriving to the center (dashed line) just before the pressure maximum. Nonlinearities are becoming very important. The simulation was done with 100 mesh points per wavelength, starting with a static density $\rho_{\rm st} = \rho_0$.

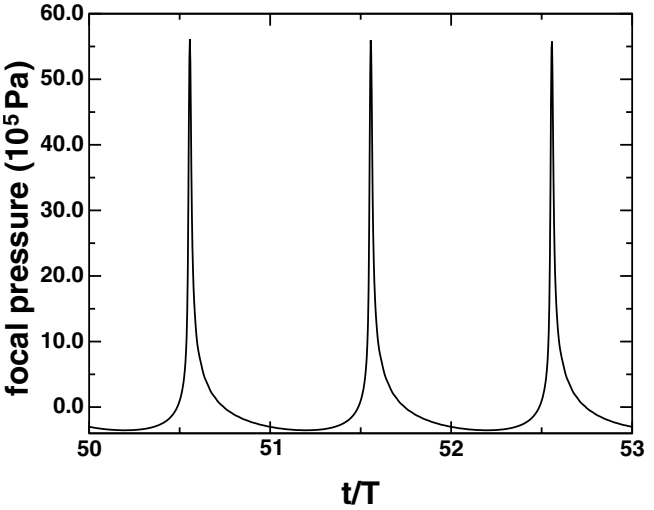

Fig. 13. Focal pressure for an oscillation $\Delta x_0 = 7$ nm. Nonlinearities are becoming very important. The simulation was done with 100 mesh points per wavelength, starting with a static density $\rho_{\rm st} = \rho_0$.

one clearly sees the formation of sharp fronts (Fig. 12). At the center, the positive swings of the pressure are now very sharp compared to the negative ones (Fig. 13). The shape of the negative swings is also clearly asymmetric in time.

It would be tempting, in order to reduce the computational effort, to assume that nonlinearities play a role only in the last wavelengths. Then, one could simulate a reduced box with radius $L_{\rm red}$, and take as an input condition:

$$\Delta x_{\rm red} = \Delta x_{\rm exp} \frac{L_{\rm exp}}{L_{\rm red}} \qquad (20)$$

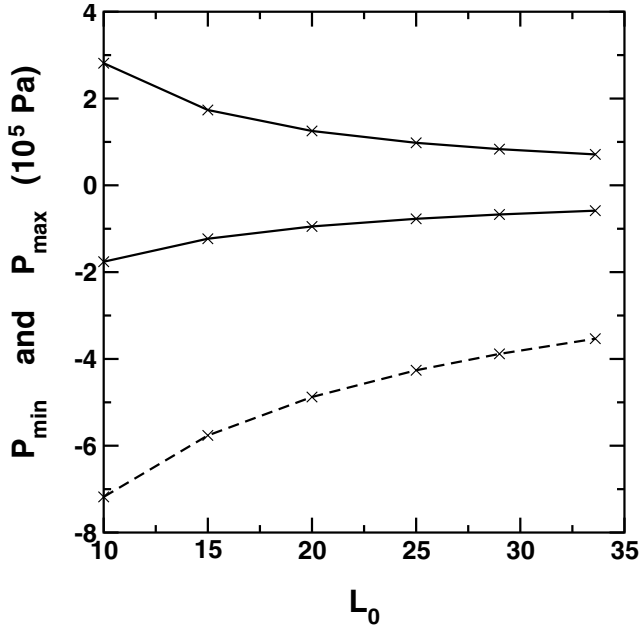

Fig. 14. Minimal and maximal focal pressure, as a function of the cell radius. The product $L_{\rm red} \times \Delta x_{\rm red}$ is constant for each curve. Solid lines (resp. dashed lines) correspond to an experimental oscillation amplitude $\Delta x_{\rm exp} = 0.7$ nm (resp. 7 nm). One of the curves (P_{max} for 7 nm) is not visible, as it varies from 2.80×10^9 Pa to 1.06×10^7 Pa! In all cases, the simulation was done with about 350 points per wavelength.

where $\Delta x_{\rm exp}$ is the experimental oscillation amplitude of the transducer, and $L_{\rm exp}$ its radius. Actually, this is fine as long as nonlinearities do not play a role at all, i.e. as long as the focal pressure is sinusoidal. In all other cases, as this is shown in Figure 14, nonlinearities are built through the whole propagation process, and one cannot neglect them even far from the center, without modifying the focal pressure. This could also be seen in the shock length analytic expression (11), which is directly proportional to the cell radius. In Figure 14, we have performed simulations with various cell radii, corresponding to the same experimental oscillation amplitude on the ceramic. As the cell radius increases, both the positive and negative pressure swings decrease (in absolute values). Nonlinearities make it more difficult to reach extreme values. Thus in all the simulations presented in this paper, we have simulated the whole experimental cell, with radius 8 mm.

We have seen in Figure 13 that positive pressure peaks can reach tremendously high values. Of course one may wonder whether this is actually physical. The obvious answer is no, but it is worth discussing this point in some details.

The solution of the problem as we defined it in Section 2.1 becomes singular when the shock reaches the center of the sphere, and positive peaks actually diverge in the simulations as the spatial discretization step δr is decreased at constant CFL number (see Fig. 15). For each fixed δr, one still finds a finite focal pressure, as it is defined as an average over the central cell - with radius $\delta r/2$.

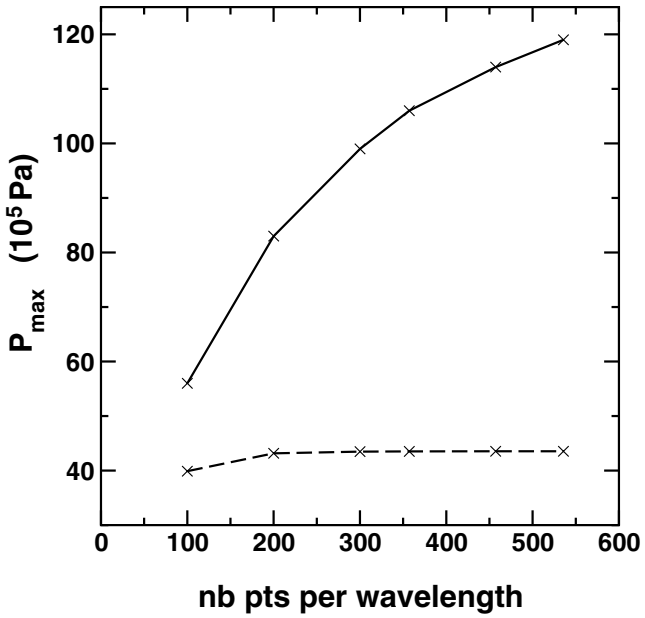

Fig. 15. Maximum of the focal pressure (solid line) as a function of the number of points per wavelength, for an oscillation amplitude $\Delta x_0 = 7.0$ nm. For comparison, the dashed line gives the pressure after a spatial average weighted by a Gaussian with waist 7 μm.

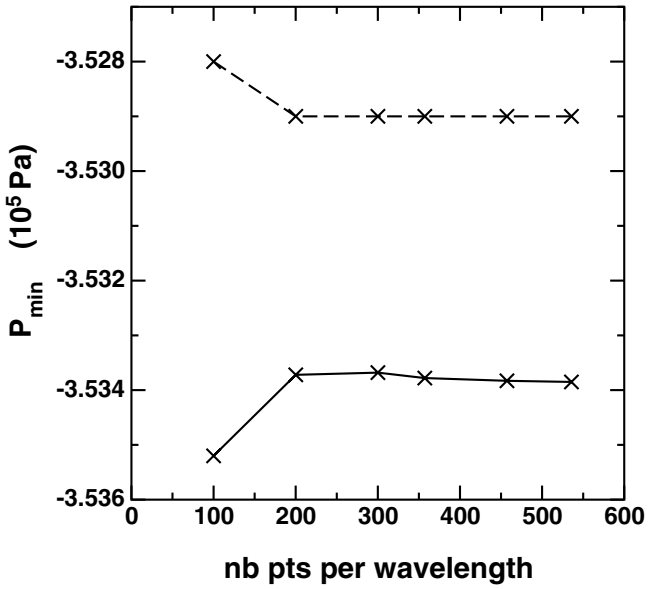

Fig. 16. Minimum of the focal pressure with the parameters of Figure 15.

We check in Figure 16 that the minimal pressure does converge for a decreasing δr.

A first remark is that this singularity involves only a very small region around $r = 0$ (ultimately, it is singular only in $r = 0$). In the experiment, one cannot measure the pressure exactly in $r = 0$, but rather over the whole region reached by the laser beam (see Sect. 3). The intensity of the laser beam through its cross section is Gaussian, with a beam waist (half width) of about 7 μm. In order to take

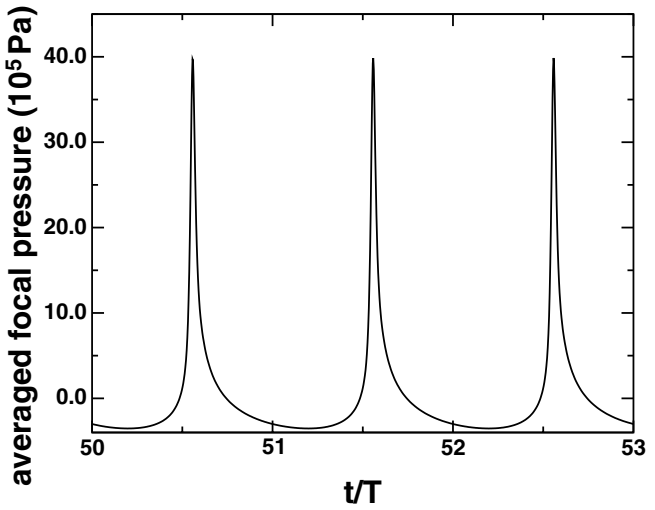

Fig. 17. Averaged focal pressure for an oscillation $\Delta x_0 = 7$ nm. The spatial average is weighted by a Gaussian with waist 7 μm. This is to be compared with Figure 13.

this averaging effect into account in the simulation, we have also computed a spatial average value of the pressure weighted by a Gaussian of waist 7 μm (Fig. 17). Positive pressure peaks are lowered, while the negative swing is not very sensitive to the averaging process, as gradients are much weaker than during the positive swing. But above all, one now obtains extrema which are converging as $\delta r \to 0$ (Fig. 15).

However, it is not enough to rule out the singularity by an averaging process. Actually, the singularity is not expected to hold as such in a more realistic description. First, the third Euler equation for energy should also be taken into account in this regime, as well as regularization mechanisms (dispersion, dissipation). Secondly, in the experiment, we expect diffraction, and the fact that actually the flux is not zero at the focal point, to break the geometrical symmetry. Making quantitative estimates of these effects is not simple, and is postponed to future work. Finally, even with averaging, positive pressure peaks in Figure 17 are still so high that they are far above the solidification pressure (2.53×10^6 Pa at $T = 0$). Our recent experiments show that indeed acoustic waves can trigger crystallization, not only cavitation [3]. However in our simulations, the possible crystallization has not been taken into account.

As a conclusion, the value of the positive pressure swings is not expected to be reliable for high amplitudes of the transducer surface. But we checked, using different types of numerical regularization of the shocks (an example is given in the next section), that even if it affects the maximal pressure, it has no effect on the negative swings, and thus it is still possible to use our simulations to draw conclusions for negative pressures.

In Figures 18 and 19, we show the density profile and focal pressure obtained for $\Delta x_0 = 30$ nm, a value which can be reached in cavitation experiments. Figure 18 illustrates how shocks are formed when the wave arrives near the focal point. The amplitude of the shock increases

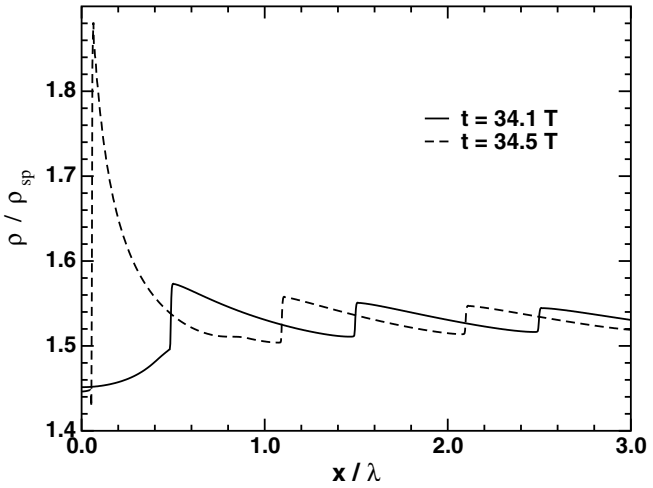

Fig. 18. Density profile for an oscillation $\Delta x_0 = 30$ nm. Shocks form near the focal region. The simulation was done with about 350 points per wavelength.

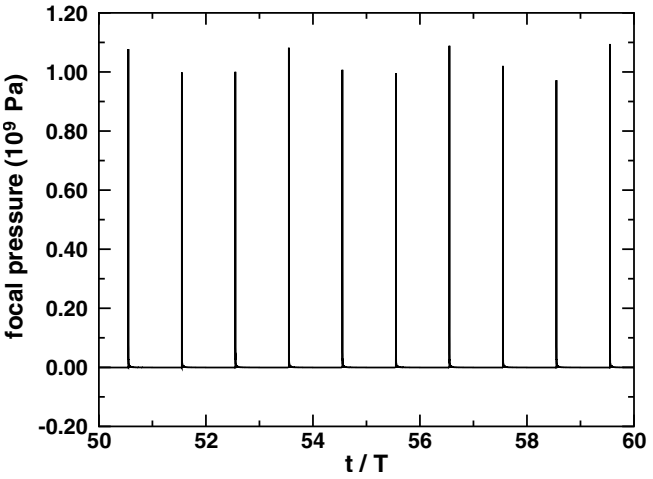

Fig. 19. Focal pressure for an oscillation $\Delta x_0 = 30$ nm. The simulation was done with about 350 points per wavelength.

when the shock itself arrives at the focal point, leading to tremendous pressure maxima in the simulations (here about 1.2×10^9 Pa). This is of course unphysical, as we just discussed, but the important point is that the minimum (negative) pressure does not depend on the value of the maximal pressure. Thus it is still possible to calculate a minimum pressure value and compare with experiments.

Figure 20 shows the amplitude of the transducer oscillation which is necessary to reach a given minimal pressure at the center, starting from a static pressure $P_{\rm st}$. Actually, the variable we plot is rather $P_{\rm st}$ as a function of $\rho_{\rm st}\Delta x_0$, in order to see the departure from the linear theory:

$$P_{\rm min} = P_{\rm st} - \omega^2 L_{\rm exp}\rho_{\rm st}\Delta x_0. \qquad (21)$$

Our interest in such a curve came from a first version of the experiment, for which it was not possible to measure the focal pressure. Still, we were able to measure the oscillation amplitude necessary to obtain cavitation for various initial static pressures, i.e. we could plot a curve such as

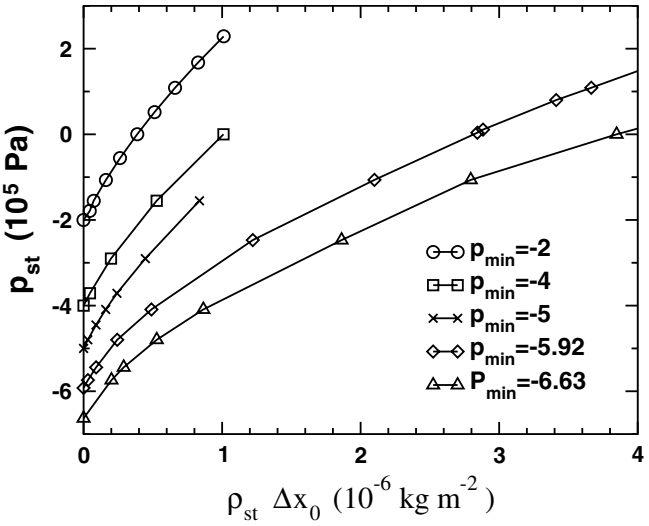

Fig. 20. Static pressure, as a function of the oscillation amplitude for which the minimal focal pressure is equal to a given value $P_{\rm min}$, multiplied by the static density. Each curve corresponds to a different value of $P_{\rm min}$ (in 10^5 Pa).

those of Figure 20, for the special case $P_{\rm min} = P_{\rm cav}$, the cavitation pressure. However this could be done only for positive static pressures, while we were interested in the zero amplitude value of the curve, for which static pressure and cavitation pressure should be the same. Thus simulations are useful to determine which kind of extrapolation should be used for negative static pressure values.

It is interesting to see that the effect of nonlinearities is to bend such curves in a concave way (Fig. 20). In reference [2], the sign of this curvature was used to show that a linear extrapolation provides an upper bound of the cavitation pressure. Whether the shock formation affects the nucleation mechanism is an open question. If we try to plot the same oscillation amplitude as a function of the static density in the cell (Fig. 21), instead of the static pressure (Fig. 20), nonlinearities are even more pronounced, as would have been expected from the equation of state (a concave function of a concave function is still more concave).

More important for the validation of our numerical methods is that we later succeeded in measuring at the focal point the temporal signal itself. As explained below, this was done in a quasi-spherical geometry and very good agreement was found between theory and experiments.

3 Experiments

A hemispherical piezoelectric transducer is held against a clean glass plate. In a first approximation, the glass reflects the sound wave so that this is equivalent to a full spherical geometry. The main interest of the glass plate is that it allowed us to measure the instantaneous density at the center from the reflection of light at the glass/helium interface.

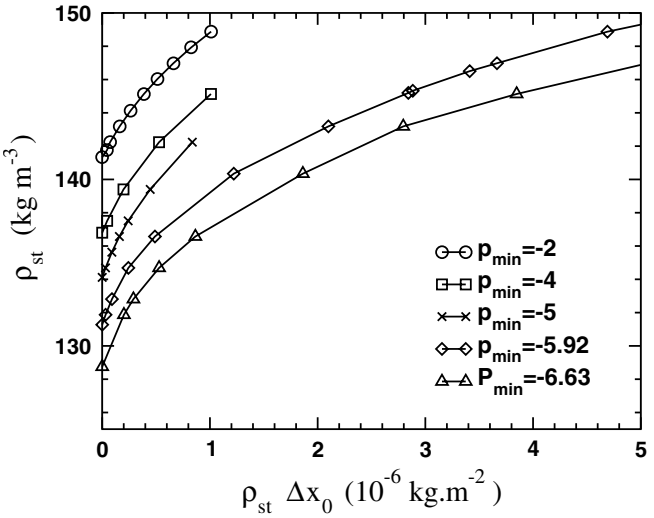

Fig. 21. Same figure as Figure 20, except that the static pressure is replaced by the corresponding static density. The curvature of the function is enhanced by using this variable.

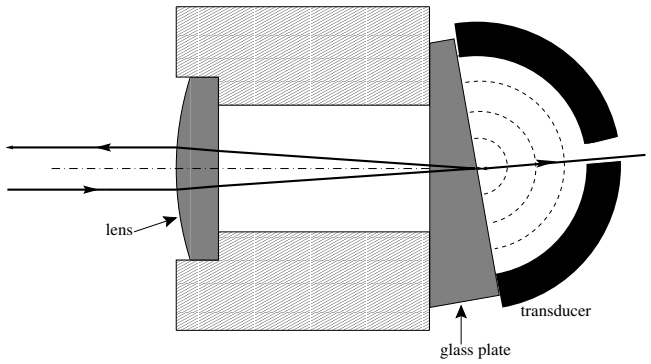

Fig. 22. The experimental set-up which is immersed in liquid helium, inside the experimental cell. At the center of the hemispherical transducer, the amplitude of the sound oscillation is measured from the intensity of the reflected light. The transmitted light is used to detect the possible nucleation of bubbles or crystallites.

3.1 Experimental method

Our experimental method is described in full details elsewhere [24,25]. Let us only summarize it here. The transducer radius is 8 mm and its thickness is 2 mm. It resonates in a thickness mode at $f = 1.019$ MHz. At this frequency, it has a minimum impedance $Z = 22\ \Omega$. Its quality factor is $Q = 50 \pm 5$ when immersed in liquid helium at 25×10^5 Pa. We usually pulse it with bursts of 6 oscillations. Thanks to a dilution refrigerator, we can run the experiment between 30 mK and 1.5 K, at static pressures from 0 to 25×10^5 Pa. Figure 22 shows our optical setup: a brass piece holds a lens and a wedged glass plate in liquid helium. The transducer is pressed against the plate. Thanks to the lens, the radius of the laser waist is 7 μm, so that the spatial resolution is about 14 μm. This is small compared to the size of the acoustic focal region which is set by the acoustic wavelength at 1 MHz: from 240 μm at 0 Pa to 360 μm at 25×10^5 Pa. The 2 degrees wedge of the glass plate avoids interferences with reflections on its front face. A hole in the transducer allows the transmitted light to be analyzed on the other side of the cryostat.

We use an Ar^+ laser and we carefully focus it at the center of the acoustic focal region. The transmitted light is collected by a photomultiplier tube (PMT) and used to detect nucleation events one by one. The light which is reflected at the glass/helium interface is separated from the incident beam by means of a semi-transparent plate. Its intensity is proportional to the normal reflectance R at the glass/helium interface, which depends on the refraction index of helium, i.e. on its density as it is well known from the Clausius-Mossoti relation. Note that, due to a large acoustic impedance mismatch, the sound transmission into the glass plate is negligible, so that the index of the glass can be considered as constant during the measurement. Furthermore, the acoustic radiation pressure on the center of the plate is small so that no significant flexion of this plate occurs. Finally, the reflected intensity is not sensitive to the exact location of the glass/helium interface. A careful calibration (see Refs. [24,25]) allowed us to extract the absolute amplitude of the acoustic wave at the center of the acoustic focal region from the ac-component of the reflected light.

3.2 Comparison with calculations

Figure 23 shows two recordings obtained at 0.1K with respective excitation amplitudes of 9.05 and 20.4 V on the transducer. In the cell, the static pressure is 9.80×10^5 Pa, corresponding to a static density $\rho = 158.51\,\mathrm{kg\,m^{-3}}$. At 20.4 V, the density oscillation is found asymmetric: negative swings are broader with a smaller amplitude than positive swings. Moreover, the negative swings are not symmetric in time. This recording at intermediate pressure and moderate amplitude has been chosen because the signal shape is not modified by any nucleation of crystals or bubbles.

We can compare the experimental recordings with the numerical calculations described in Sections 2.3 and 2.4. Simulations are performed with the same static pressure as in the experiment. Then there is only one free parameter in the simulation (the oscillation amplitude Δx_0) in order to adjust both the amplitude and the shape of the signal. The adjustment with the experimental signal is made only on the central oscillation of the latter. Indeed, in the experiment, the transducer is excited with an electrical burst of six oscillations. Longer bursts would dissipate too much heat in this low temperature experiment. Such short bursts also force nucleation to occur at a well defined time. This is because the transducer has a finite quality factor $Q \approx 50$, so that the amplitude of the sound wave increases during the first six periods and slowly decreases afterwards. The numerical result is used in the steady regime, after its initial transient, but it does not matter for the comparison. As can be seen, we find a very good agreement for numerical oscillation amplitudes

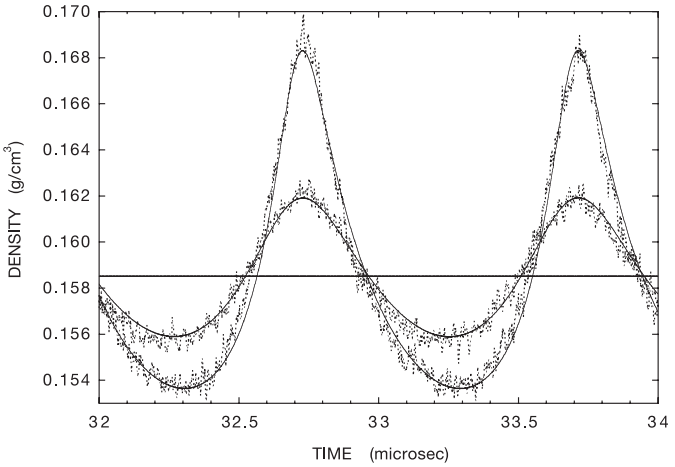

Fig. 23. Two recordings of sound wave amplitudes respectively corresponding to excitation voltages 9.05 and 20.4 V on the transducer. The static density is $\rho = 0.15851$ g/cm^3 (horizontal line), corresponding to a static pressure $P_{stat} = 9.80 \times 10^5$ Pa. The asymmetry of the oscillations is well reproduced by the numerical calculations performed for $\Delta x_0 = 3$ and 6 nm. The numerical focal density (solid lines) is weighted by a Gaussian with waist 7 μm. Simulations are performed with 350 mesh points per wavelength.

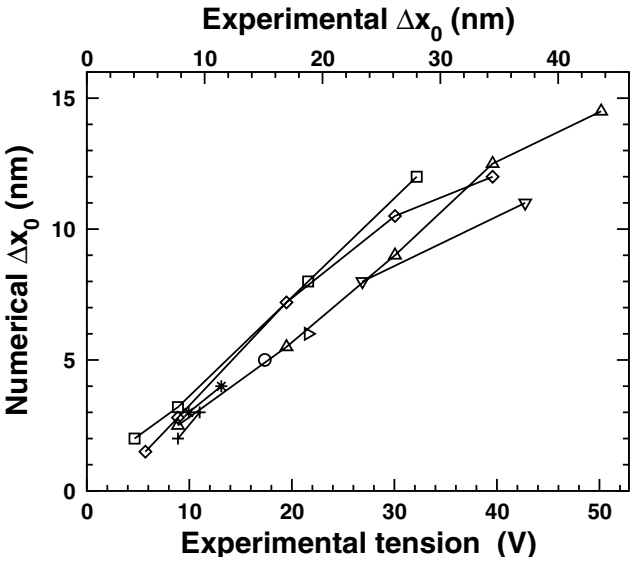

Fig. 24. Oscillation amplitude Δx_0 for which the simulation fits the experimental signal, as a function of the experimental applied voltage. These results are obtained for different static pressures, i.e. 0.110 ($\star$), 0.800 ($\circ$), 4.3 ($\square$), 5.1 ($\diamond$), 9.8 ($\triangle$), 15.4 ($\triangledown$), 22 ($\triangleright$), and 25.3 ($+$) $\times 10^5$ Pa. We also indicate as a second x-axis the estimate for the oscillation amplitude given by (29) which is obtained from independent physical arguments.

$\Delta x_0 = 3$ and 6 nm: both the asymmetry with respect to the horizontal axis and the asymmetry in time are well reproduced by the calculation.

Similar adjustments with several recordings, for different oscillation amplitudes and different static pressures, are summarized in Figure 24. All the points come from the WENO scheme. This allowed us to check the convergence of the results for a decreasing spatial step δr, thus beyond the limit of stability of the finite difference scheme of Section 2.3.1. For $\Delta x_0 < 6$ nm, most points have been obtained with both schemes allowing us to check that they give the same results for this range of amplitudes. For each adjustment, the numerical amplitude obtained by fitting the central oscillation is associated to the experimental voltage applied to the transducer. In Figure 24, we also indicate as a second x-axis the estimate given by equation (29) for the oscillation amplitude Δx_0. This estimate is obtained independently from the simulations, as will be detailed below. It is referred to as the experimental oscillation amplitude in the figure. If the estimate and the numerical adjustment were in perfect agreement, one would expect a slope equal to one in Figure 24. Actually, we find that both methods give different results, and this will be discussed below. The adjustment between experimental signals and numerical simulations yields the following calibration:

$$\frac{\Delta x_0}{V} = 0.30 \pm 0.02 \text{ nm V}^{-1}. \tag{22}$$

It is interesting to compare this value with an estimate from the measurement of the electrical characteristics of the ceramic. Let us summarize the derivation of this estimate, which is given in reference [2]. Indeed, the quality factor is simply related to the ratio of the acoustic energy $E_{\rm ac}$ which is stored during one period to the average dissipated power $V^2/(2Z)$:

$$Q = 4\pi f \frac{E_{\rm ac}\, Z}{V^2}, \tag{23}$$

and the acoustic energy can be evaluated as follows. Let us call $R_{\rm m}$ the mean radius of the transducer and $2e$ its thickness. For a resonance in a thickness mode, one can assume that the sound wave inside the transducer is a spherical wave with an elastic displacement given by

$$\Delta x = \Delta x_0 \frac{R_{\rm m} - e}{r} \sin[k(r - R_{\rm m})] \sin(\omega t), \tag{24}$$

where the wavevector $k = \pi/2e$ and $\omega = 2\pi f$.

Since $E_{\rm ac}$ is twice the average kinetic energy in the transducer [2] and the local velocity is simply the time derivative of Δx, one can integrate over the thickness and write:

$$E_{\rm ac} = \pi \rho_{\rm t} \omega^2 {\Delta x_0}^2 (R_{\rm m} - e)^2 e \tag{25}$$

where $\rho_{\rm t}$ is the transducer density. After expressing $E_{\rm ac}$ in terms of the mass of our transducer, we obtain

$$E_{\rm ac} = \frac{M}{4} \omega^2 {\Delta x_0}^2 \frac{(R_{\rm m} - e)^2}{R_{\rm m}^2 + \frac{e^2}{3}} \tag{26}$$

where $M = 7.510^{-3}$ kg. Note that the last factor was forgotten in reference [2]. Finally, we can express the

displacement Δx_0 as a function of the applied voltage:

$$\Delta x_0 = V \left(\frac{2Q}{\omega^3 M Z}\right)^{1/2} \frac{R_\mathrm{m}}{R_\mathrm{m} - e} \sqrt{1 + \frac{e^2}{3R_\mathrm{m}^2}}. \qquad (27)$$

The above equation leads to $\Delta x_0/V = 1.7\,\mathrm{nm\,V^{-1}}$. However, this value would correspond to an excitation with long bursts, when the stored energy saturates. Since we excite it with bursts of six oscillations only, and since the phase is such that they start with positive swings, the maximum pressure is reached $(6 + 1/4)$ periods after time zero, and the displacement to be considered in our case is

$$\Delta x_0(6) = [1 - \exp(-12\pi/Q)] \exp(-\pi/2Q)\ \Delta x_0 \qquad (28)$$

We find $\Delta x_0(6) = 0.513\,\Delta x_0$ with Δx_0 given by equation (27), and our final prediction is

$$\frac{\Delta x_0(6)}{V} = 0.88\ \mathrm{nm\,V^{-1}}. \qquad (29)$$

The above value has the right order of magnitude but it is three times larger than that given by the fit of our numerical calculations (Eq. (22)). There are several assumptions in the above analysis which can be claimed as responsible for this discrepancy. We list them starting with those that we expect to be the most relevant:

a - the resonance in a thickness mode may be coupled to flexion modes, in which case the efficiency of the transducer can easily be reduced;
b - there is a small hole in the center of the transducer which allows the transmitted light to be analyzed;
c - the sound wave in the transducer cannot be strictly spherical, since there must be edge effects near its free equator;
d - the reflection by the glass plate is not perfect so that our closed hemispherical geometry is not strictly equivalent to a full spherical geometry. Once more this should reduce the efficiency of the transducer;
e - some of the emitted energy is lost in the various pieces which hold it in the cell;
f - there is also some uncertainty of order 10% in the measurement of Z and Q.

As a result, we consider the value $0.3\ \mathrm{nm\,V^{-1}}$ as a very useful calibration of the efficiency of our transducer, in qualitative agreement with a simple estimate.

4 Conclusions and perspectives

In this article, we have presented analytic and numerical calculations of the focusing of a spherical acoustic wave. We have shown that shocks are generated in this geometry and we have obtained an analytic estimate for the shock length based on the characteristics method. Then, in order to perform full numerical simulations of the focusing process, we have used a WENO scheme to treat shocks. We then showed that our method is validated by a comparison with experimental measurements in a quasi-spherical geometry. We have measured a wave distortion which is well reproduced by our calculation and the analysis of its dependence on the excitation amplitude has led us to a very useful calibration of the efficiency of our transducers.

We consider this work as a first step only, and we plan to extend it to a hemispherical geometry for two important reasons. Indeed, in order to study the homogeneous nucleation of bubbles in stretched fluids (under negative pressure) or that of crystals in pressurized fluids, we need to eliminate the effect of walls. This is achieved by using hemispherical transducers which focus acoustic waves away from any walls [1,2]. In such experiments, since we have no probe in the acoustic focal region where nucleation takes place, there is a difficult problem of calibration of the sound amplitude, for which any reliable calculations would be very useful. Of course, the calculation in a hemispherical geometry is much more difficult because it is two-dimensional (it depends on both the radial distance and the polar angle). Now that the method is known for the treatment of shocks, the 2-D calculations should be tried. Furthermore, we have estimated the amplitude of nonlinear effects in the hemispherical geometry [2], and found them to be much smaller than in the spherical geometry, though lower pressures seem to be reached. This is interesting in itself and should be tested numerically. One physical explanation could be that the local condition at the center is different: by symmetry, the spherical geometry imposes that the center is a node for the fluid velocity. In the hemispherical geometry, there is no reason why it should be so. On the contrary, the sound wave could even create a flow at the center with non vanishing averaged value. This phenomenon is known in the literature as acoustic streaming. This symmetry difference might lead to a different amplitude for the nonlinear effects. It would be very interesting to study this phenomenon numerically.

Another direction of research would deal with the interaction between shocks and nucleation. Until now, all theories predicting the nucleation threshold ignore the presence of very steep gradients. This is not necessarily justified.

We are grateful to H. Lambaré for his contribution to the calculations in their early stage. C.A. would like to thank Frédéric Coquel for interesting discussions.

Appendix A: Theoretical prediction of the shock length by the characteristics method

A.1 Characteristic equations

The system of Euler equations (2) is of the form

$$\partial_t v_i + A_{ij} \partial_r v_j = b_i, \qquad (30)$$

with $\mathbf{v} \equiv (\rho, u)$ and $\mathbf{b} = (-\theta\rho u/r, 0)$. The matrix

$$A = \begin{pmatrix} u & \rho \\ \frac{c_s^2}{\rho} & u \end{pmatrix}$$

has two eigenvalues $\mu_+ = u+c_\mathrm{s}$ and $\mu_- = u-c_\mathrm{s}$ associated with the left eigenvectors

$$\mathbf{l}_+ = \begin{pmatrix} c_\mathrm{s}/\rho & 1 \end{pmatrix}, \\ \mathbf{l}_- = \begin{pmatrix} -c_\mathrm{s}/\rho & 1 \end{pmatrix}. \tag{31}$$

If we apply $\mathbf{l}_k$ on the left of equation (30), we obtain

$$\mathbf{l}_k . \left[\frac{d\mathbf{v}}{dt} - \mathbf{b} \right] = 0, \tag{32}$$

where

$$\frac{d}{dt} = \partial_t + \mu_k \partial_r.$$

Thus the derivative d/dt is taken along a curve $r = x(t)$ with slope $dx/dt = \mu_k$ everywhere (μ_k itself being a function of r and t via v). By definition, this curve is called a k-th characteristic and is denoted by $\mathcal{C}^{(k)}$. There is a whole family of $\mathcal{C}^{(k)}$ characteristics, covering the whole space, each curve being determined, for example, by the initial conditions.

The leftmost term of equation (32) can be integrated and the equation becomes

$$\frac{d}{dt} \left[C_\mathrm{o}(\rho - \ln \rho) \pm u \right] + \theta \frac{C_\mathrm{o}(\rho-1)u}{r} = 0, \tag{33}$$

where again the time-derivative is taken along a characteristic curve.

We call Riemann invariants the quantities

$$I_\pm \equiv C_\mathrm{o}(\rho - \ln \rho) \pm u \tag{34}$$

appearing in equation (33).

A.2 Lower bound for the shock length

Considering the geometry and notations of Section 2.2.2, we calculate at what time the first characteristic $\mathcal{C}_0^{(-)}$ emitted by the piston at $t = 0$ is cut by another characteristic $\mathcal{C}_i^{(-)}$. This is the signature of a shock forming. The calculation assumes that it is the first shock ever formed in the cell.

As $\mathcal{C}_0^{(-)}$ is first cut by characteristics $\mathcal{C}^{(-)}$ emitted at early times, and almost parallel to $\mathcal{C}_0^{(-)}$, we perform the following change of variable. Instead of r, the location of any point will be given by its distance η to a point moving on the characteristic $\mathcal{C}_0^{(-)}$, taken at the same time:

$$\eta = L_0 - c_\mathrm{st} t - r. \tag{35}$$

The characteristic equations (33) have to be written in the new coordinates (η, t). Besides, we would like to eliminate u and ρ from the equations so that the only remaining unknowns would be the Riemann invariants I_+ and I_-. Following [7], we have $d\eta/dt = -(u \pm c_\mathrm{s} + c_\mathrm{st})$ and $u = (I_+ - I_-)/2$. But unlike in reference [7], the density ρ and thus the sound velocity can only be expressed in terms of I_+ and I_- by inverting the relation

$$I_+ + I_- = 2C_\mathrm{o}(\rho - \ln \rho) \equiv 2I(\rho), \tag{36}$$

leading to

$$\rho = \mathcal{I}^{-1} \left(\frac{I_+ + I_-}{2} \right), \tag{37}$$

with $\mathcal{I}^{-1}(x) = W(e^{x/C_\mathrm{o}})$, where W is the Lambert W function [26]. The characteristic equations now read

$$\partial_t I_+ - \left\{ \frac{I_+ - I_-}{2} + C_\mathrm{o} \left[\mathcal{I}^{-1} \left(\frac{I_+ + I_-}{2} \right) - 1 \right] + c_\mathrm{st} \right\} \partial_\eta I_+ \\ + \frac{2}{L - c_\mathrm{st} t - \eta} \left(\frac{I_+ - I_-}{2} \right) C_\mathrm{o} \left[\mathcal{I}^{-1} \left(\frac{I_+ + I_-}{2} \right) - 1 \right] = 0 \tag{38}$$

$$\partial_t I_- - \left\{ \frac{I_+ - I_-}{2} - C_\mathrm{o} \left[\mathcal{I}^{-1} \left(\frac{I_+ + I_-}{2} \right) - 1 \right] + c_\mathrm{st} \right\} \partial_\eta I_- \\ + \frac{2}{L - c_\mathrm{st} t - \eta} \left(\frac{I_+ - I_-}{2} \right) C_\mathrm{o} \left[\mathcal{I}^{-1} \left(\frac{I_+ + I_-}{2} \right) - 1 \right] = 0. \tag{39}$$

We search for a solution under the form

$$I_+(\eta, t) = \sum_{m=0}^{\infty} I_+^{(m)}(t) \eta^m, \\ I_-(\eta, t) = \sum_{m=0}^{\infty} I_-^{(m)}(t) \eta^m. \tag{40}$$

We choose the lowest order terms $I_+^{(0)}$ and $I_-^{(0)}$ equal to their value in the fluid at rest $I_+^{(0)} = I_-^{(0)} = C_\mathrm{o}(\rho_\mathrm{st} - \ln \rho_\mathrm{st})$. Then if we write equations (38–39) at lowest order, all the terms in the second equation vanish. In the first equation, both the first and last terms disappear. The remaining term leads to

$$I_+^{(1)} = 0. \tag{41}$$

This is not very surprising, as I_+ corresponds to the characteristics moving from the fluid at rest into the perturbed region. Taking (39) to the next order, we obtain an equation for $I_-^{(1)}$

$$\frac{dI_-^{(1)}}{dt} + \frac{1}{t - L_0/c_\mathrm{st}} I_-^{(1)} + \mathcal{K} \left[I_-^{(1)} \right]^2 = 0, \tag{42}$$

where

$$\mathcal{K} \equiv \frac{1}{2} \left(\frac{2\rho_\mathrm{st} - 1}{\rho_\mathrm{st} - 1} \right). \tag{43}$$

This equation can be solved using a change of variables $\overline{I_-} \equiv 1/I_-^{(1)}$. The solution yields

$$I_-^{(1)}(\tau) = \frac{I_-^{(1)}(0)}{(1-\tau) \left[1 - \mathcal{K} \frac{L_0}{c_\mathrm{st}} I_-^{(1)}(0) \ \ln(1-\tau) \right]}, \tag{44}$$

with

$$\tau \equiv \frac{c_{\rm st}}{L_0} t. \tag{45}$$

We have now to determine the initial value $I_-^{(1)}(0)$. It refers to small t, rather than t exactly equal to zero.

To determine its value, we calculate for small time t the variation of I_- between point $A = (r,t) = (L_0 - c_{\rm st}t, t)$ which sits on the first characteristic $\mathcal{C}_0^{(-)}$, and point $B = (r,t) = (r_p(t), t)$ where $r_p(t)$ is the location of the piston at time t.

At A, the fluid is at rest. We have $I_- = I_-^{(0)}$ and $\eta = 0$.

At B, for t small, $r \simeq L_0$ and thus $\eta \simeq -c_{\rm st}t$. Besides, $I_- = C_{\rm o}(\rho - \ln\rho) - u$ where u is equal to the velocity of the piston $v_p(t) = -\Delta v_0 \sin(\omega t) \simeq -\Delta v_0 \omega t$. If we expand $\rho(r_p(t),t) = \rho_{\rm st} + \alpha t$ (where α is unknown), then replacing into I_- and expanding in t yields

$$\begin{aligned} I_- &= C_{\rm o}(\rho_{\rm st} - \ln\rho_{\rm st}) + C_{\rm o}\alpha t - C_{\rm o}\frac{\alpha}{\rho_{\rm st}} t + \Delta v_0 \omega t \\ &= I_-^{(0)} + \left(\frac{c_{\rm st}}{\rho_{\rm st}}\alpha + \Delta v_0 \omega \right) t. \end{aligned}$$

Comparing this relation with the expansion

$$I_- = I_-^{(0)} + \eta I_-^{(1)} \simeq I_-^{(0)} - c_{\rm st} I_-^{(1)} t, \tag{46}$$

gives

$$I_-^{(1)} = -\frac{\alpha}{\rho_{\rm st}} - \frac{\Delta v_0}{c_{\rm st}}\omega. \tag{47}$$

On the other hand, an expansion of (37) in powers of η gives

$$\alpha t = \rho_{\rm st}\rho_{\rm st} = \frac{c_{\rm st}}{\rho_{\rm st}} \left(\eta \frac{I_-^{(1)}}{2} \right) t. \tag{48}$$

The elimination of α between the above two equations yields

$$I_-^{(1)}(t=0) = -2\frac{\Delta v_0 \omega}{c_{\rm st}}. \tag{49}$$

The time at which $I_-^{(1)}$ becomes infinite (see Eq. (44)) gives an upper bound $t_{\rm shock}$ for shock formation. It is only an upper bound because some other terms of the expansion (40) in η may explode before $I_-^{(1)}$. We find

$$t_{\rm shock} \le \frac{L_0}{c_{\rm st}} \left\{ 1 - \exp\left[-\frac{c_{\rm st}^2}{2L_0\omega\Delta v_0} \frac{\rho_{\rm st} - 1}{\rho_{\rm st} - \frac{1}{2}} \right] \right\} \le \frac{L_0}{c_{\rm st}}. \tag{50}$$

As the corresponding shock distance $r_{\rm shock}$ is measured from the center of the sphere, a lower bound for $r_{\rm shock}$ is

$$L_0 \ge r_{\rm shock} \ge L_0 \exp\left[-\frac{c_{\rm st}^2}{2L_0\omega\Delta v_0} \frac{\rho_{\rm st} - 1}{\rho_{\rm st} - \frac{1}{2}} \right] > 0. \tag{51}$$

All the above calculations are valid for small η, i.e. only for characteristics not too far from $\mathcal{C}_0^{(-)}$. These are the characteristics emitted by the initial motion of the piston.

Appendix B: The WENO scheme in more details

To reconstruct the numerical flux $(\overline{F}^n_{i+1/2})$ evaluated at the cell interface $(r_{i+1/2})$ (see Eq. (17)), a scheme with a discontinuity-capturing feature must be employed to prevent oscillations in the vicinity of the shock wave. Following a previous study [23] on the capability of some recent high-order shock capturing schemes to recover basic fluid mechanics phenomena, the numerical flux has been evaluated by means of a Essentially Non-Oscillatory (ENO) family scheme [20–22]. The numerical flux is approximated using polynomial reconstruction over several grid points (the set of these points is named "stencil") around the cell boundaries. We shall now describe this reconstruction of the fluxes in details.

As in many schemes devoted to computations involving shocks, the WENO scheme uses the Riemann invariants as variables. Computing the evolution of these variables requires to know their values not only on integer space coordinates, but also at some intermediate locations. An extrapolation from integer positions is thus necessary and this is where the fundamental idea of WENO schemes comes in.

• Change of variables:

For simplicity and accuracy purposes, the discretization of the Euler flux is based on a polynomial reconstruction applied on the local characteristic variables (Riemann invariants, see Sect. 2.2.1) since the equations recover the scalar form. Then, the propagation directions can easily be followed in the characteristic plane. In order to perform this change of variables, the method is the same as in Appendix A. First one linearizes the Euler equations and finds the eigenvectors of the Euler flux Jacobian evaluated at the cell interface $((\partial F/\partial Q)_{i+1/2})$. Note that, as we are now using the Euler equations in conservative form (3) instead of (2), the Jacobian differs from the one given in Appendix A (matrix A), and now reads

$$\partial F/\partial Q = \begin{pmatrix} 0 & 1 \\ \dfrac{-q^2}{\rho^2} + c_s^2 & 2\dfrac{q}{\rho}\cdot \end{pmatrix} \tag{52}$$

In order to compute $(\partial F/\partial Q)_{i+1/2}$ then the eigenvalues $(\mu^k_{i+1/2})$, and the left $(\mathbf{l}^k_{i+1/2})$ and right $(\mathbf{r}^k_{i+1/2})$ eigenvectors $(k \in \{1,2\})$– the conservative variables Q^n_i must be evaluated at the cell interface $r_{i+1/2}$. As these variables do not vary linearly in the cell if a shock is present, one cannot use a simple arithmetic or geometric average, but should rather use a Roe average, whose description can be found in [27]. This ensures the consistency of the scheme, i.e. that $(\partial F/\partial Q)_{i+1/2}$ converges towards $(\partial F/\partial Q)_i$ when δx tends to zero.

The numerical Euler flux is then projected onto the left eigenvector matrix $\mathrm{l}_{i+1/2} = (\mathbf{l}^1_{i+1/2}, \mathbf{l}^2_{i+1/2})$. The scalar ENO reconstruction procedure is applied to the projected fluxes [21]. In the physical domain, the numerical Euler

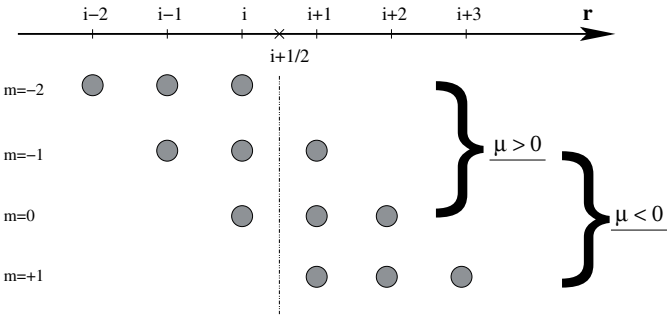

Fig. 25. Sketch of all the stencil candidates to recover a third-order reconstruction ($p = 3$) at the cell interface $r_{i+1/2}$. The eigenvalue μ stands for the extrapolated value $\mu^k_{i+1/2}$.

flux is then obtained by a projection onto the right eigenvector matrix ($\mathbf{r}_{i+1/2} = \mathbf{l}^{-1}_{i+1/2}$) and reads:

$$\overline{F}_{i+1/2} = \sum_{k=1}^{2} \left[{f^{\mathrm{ENO}}}^k_{i+1/2} \cdot \mathbf{r}^k_{i+1/2} \right] \qquad (53)$$

where ${f^{\mathrm{ENO}}}^k_{i+1/2}$ stands for the scalar ENO reconstruction, which will be defined below.

• Extrapolation of variables at non-integer locations – the core of (W)ENO schemes:

First, we shall present the strategy used in ENO schemes [21]. For a given non integer location, there are several ways to perform the extrapolation, depending on from how many integer points it will be performed, and how these points will be located with respect to the non-integer one. The set of these points is called a stencil. Figure 25 illustrates the different possible choices for a stencil of length $p = 3$. Simple finite difference schemes use a stencil defined once and for all. Here, only the length p of the stencil is fixed for a given simulation. All the $p + 1$ possible locations are considered as candidates, provided that there is at least one point adjacent to the non-integer point (see again Fig. 25).

If p denotes the order of the reconstruction, the ENO procedure [21] chooses the most regular stencil among the $p + 1$ stencil candidates. As an example for $p = 3$, we can see all the stencil candidates in Figure 25. A first selection among the $p + 1$ stencil candidates is performed according to the sign of the two eigenvalues ($\mu^k_{i+1/2}$): one keeps the p leftmost stencils for the positive or null eigenvalues and the p rightmost otherwise (Fig. 25). Indeed, the sign of the eigenvalue gives the propagation direction of the associated characteristics, and thus of the relevant information.

The regularity of the function on each of the p remaining stencils is measured by the undivided difference table [21] evaluated on each stencil and the most regular stencil is chosen among all the p stencil candidates. Of course, this stencil may be different at each time step, for each location, and for each eigenvalue $\mu^k_{i+1/2}$ ($k \in \{1, 2\}$).

Table 3. The constant coefficients ζ^p_j of the ENO reconstruction up to 5th-order.

p	m	$j=0$	$j=1$	$j=2$	$j=3$	$j=4$
1	–1	1				
	0	1				
2	–1	–1/2	3/2			
	0	1/2	1/2			
	+1	3/2	–1/2			
3	–2	1/3	–7/6	11/6		
	–1	–1/6	5/6	1/3		
	0	1/3	5/6	–1/6		
	+1	11/6	–7/6	1/3		
4	–3	–1/4	13/12	–23/12	25/12	
	–2	1/12	–5/12	13/12	1/4	
	–1	–1/12	7/12	7/12	–1/12	
	0	1/4	13/12	–5/12	1/12	
	+1	25/12	–23/12	13/12	–1/4	
5	–4	1/5	–21/20	137/60	–163/60	137/60
	–3	–1/20	17/60	–43/60	77/60	1/5
	–2	1/30	–13/60	47/60	9/20	–1/20
	–1	–1/20	9/20	47/60	–13/60	1/30
	0	1/5	77/60	–43/60	17/60	–1/20
	+1	137/60	–163/60	137/60	–21/20	1/5

The scalar ENO reconstruction is then applied on this specific stencil by means of the following polynomial development:

$${f^{\mathrm{ENO}}}^{k,m}_{i+1/2} = \sum_{j=0}^{p-1} \zeta^{p,k}_j \mathbf{l}^k_{i+1/2} \cdot F\left(Q_{i+m+j}\right) \qquad (54)$$

The integer m refers to the index of the leftmost point of the chosen stencil. The sum goes over all the points of this stencil. One recognizes the projection of the fluxes onto the left eigenvectors, that allows to go from physical variables to characteristic variables. The constant coefficients of the polynomial ($\zeta^{p,k}_j$) are calculated in order to recover a scheme of order p in regular regions. The values of ζ^p_j can be found in Table 3 up to $p = 5$.

Using this generic ENO scheme (53, 54), the Euler flux derivative is estimated with a pth-order of accuracy at best (in regular regions). However, when the stencil used at the cell interface $r_{i+1/2}$ is different from the one at $r_{i-1/2}$ (which is the case in strong gradients or shock regions), the order of accuracy decreases.

One of the drawbacks in the generic ENO scheme is the necessity to check and choose between p stencil candidates, which is quite CPU consuming. To overcome this disadvantage, we preferred using a Weighted ENO scheme (WENO) since it improves the order of accuracy of the generic ENO scheme by using a weighted combination of the p possible stencils. The weights [22] depend on the degree of regularity of the solution. In regular regions, they can be computed to achieve $(2p-1)$th-order of accuracy whereas in regions with discontinuities they are set to zero, leading to a standard ENO scheme. The WENO flux is estimated by:

$${f^{\mathrm{WENO}}}^k_{i+1/2} = \sum_{n=0}^{p-1} \omega_n \; {f^{\mathrm{ENO}}}^{k,n-p+1}_{i+1/2} \qquad (55)$$

Table 4. The constant coefficients C_n^p of the WENO reconstruction up to 5th-order, for a positive eigenvalue.

p	$n=0$	$n=1$	$n=2$	$n=3$	$n=4$
2	1/3	2/3			
3	1/10	6/10	3/10		
4	1/35	12/35	18/35	4/35	
5	1/126	10/63	10/21	20/63	5/126

where $f^{\mathrm{ENO}\,k,n-p+1}_{i+1/2}$ is the generic ENO reconstruction given by equation (54) and ω_n are the weights defined as follows:

$$\sum_{n=0}^{p-1} \omega_n = 1, \tag{56}$$

$$\omega_n = \frac{\beta_n}{\sum_{l=0}^{p-1} \beta_l} \quad \text{with} \quad \beta_n = \frac{C_n^p}{(\varepsilon + IS_n)^2} \tag{57}$$

ε is a small positive number to prevent the denominator from vanishing (hereafter we set $\varepsilon = 10^{-6}$) and IS_n is a measure of the flux function regularity for the nth ENO stencil candidates. The evaluation of the smoothness measurement (IS_n) is based on the undivided-differences and the IS_n formulation can be found in [22]. It is such that a more regular curve gives a smallest IS_n, and thus a largest weight β_n. The C_n^p coefficients are reported in Table 4 up to the order $p = 5$, for positive eigenvalues at the cell interface ($\mu^k_{i+1/2} > 0$). For the negative eigenvalue case, the WENO coefficients can be obtained by symmetry with respect to the considered cell interface ($r_{i+1/2}$).

Using this WENO scheme (55-57), the Euler flux derivative is estimated with a $(2p-1)$th-order of accuracy at best (in regular regions). Moreover, let us underline that, if the solution is regular enough, the WENO procedure recovers a high-order *centered* scheme, which is of course non-dissipative.

If the length of the stencil is $p = 3$ which is our case, the order of the scheme in regular regions is then 5. However, as the order of the scheme drops to 1 in shock regions as for any other scheme it is not interesting to increase too much the order in regular regions. As the scheme is less dissipative with $p = 4$ in the non regular regions, this could even make the results worse (indeed, in our case, $p = 4$ gave less satisfying results), since spurious oscillations may occur.

References

1. H. Lambaré, P. Roche, S. Balibar, H.J. Maris, O.A. Andreeva, C. Guthman, K.O. Keshishev, E. Rolley, Eur. Phys. J. B **2**, 381 (1998)
2. F. Caupin, S. Balibar, Phys. Rev. B **64**, 064507 (2001)
3. X. Chavanne, S. Balibar, F. Caupin, Phys. Rev. Lett. **86**, 5506 (2001)
4. M.G. Sirotyuk, Sov. Phys. Acoustics **8**, 165 (1962)
5. R.A. Roy, S.I. Madanshetty, R.E. Apfel, J. Acoust. Soc. Am. **87**, 2451 (1990)
6. S.K. Nemirovskii, Sov. Phys. Usp. **33**, 429 (1990)
7. H.P. Greenspan, A. Nadim, Phys. Fluids A **5**, 1065 (1993)
8. H.J. Maris, Phys. Rev. Lett. **66**, 45 (1991)
9. X. Chavanne, S. Balibar, F. Caupin, C. Appert, D. d'Humières, J. Low Temp. Phys. **126**, 643 (2002)
10. C. Appert, X. Chavanne, S. Balibar, D. d'Humières, C. Tenaud, in *4es Rencontres du Non-Linéaire, March 2001* (Univ. Paris Sud Paris XI Editions, 2001)
11. G.W. Waters, D.J. Watmough, J. Wilks, Phys. Lett. A **26**, 12 (1967)
12. M.F. Hamilton, D.T. Blackstock, *Nonlinear Acoustics* (Academic Press, 1998), p. 26
13. A. Jeffrey, T. Taniuti, *Nonlinear wave propagation* (Academic Press, 1964); G.B. Whitham, *Linear and Nonlinear Waves* (Wiley-Interscience, 1974)
14. L. Landau, E. Lifshitz, in *Course of Theoretical Physics, Vol. 6, Fluid Mechanics* (Pergamon Press, 1959), p. 266
15. C. Canuto, M.Y. Hussaini, A. Quarteroni, T.A. Zang, *Spectral methods in fluid dynamics* (Springer Verlag, New-York, 1988)
16. C. Bernardi, Y. Maday, *Approximations spectrales de problèmes aux limites elliptiques*, Collection Mathématiques & Applications, edited by J.M Ghidaglia, P. Lascaux (Springer Verlag, 1992)
17. R. Peyret, *Spectral methods with application to incompressible viscous flow* (Springer Verlag, 2002)
18. S.K. Lele, J. Comp. Phys. **103**, 16–42 (1992)
19. K. Mahesh, J. Comp. Phys. **145**, 332–358 (1998)
20. C.W. Shu, S. Osher, J. Comp. Phys. **77**, 439 (1988)
21. C.W. Shu, S. Osher, J. Comp. Phys. **83**, 32 (1989)
22. G.-S. Jiang, C.H. Shu, J. Comp. Phys. **126**, 202 (1996)
23. C. Tenaud, E. Garnier, P. Sagaut, Int. J. Numerical Methods Fluids **33**, 249 (2000)
24. X. Chavanne, S. Balibar, F. Caupin, J. Low Temp. Phys. **125**, 155 (2001)
25. X. Chavanne, S. Balibar, F. Caupin, J. Low Temp. Phys. **126**, 615 (2002)
26. R.M. Corless, G.H. Gonnett, D.E.G. Hare, D.J. Jeffrey, D.E. Knuth, Adv. Comp. Math. **5**, 329 (1996)
27. P.L. Roe, J. Comp. Physics **43**, 367 (1981)